frontiers | Frontiers in Remote Sensing

TYPE Original Research
PUBLISHED 12 January 2026
DOI 10.3389/frsen.2025.1703604



OPEN ACCESS

EDITED BY
Zhigang Cao,
Chinese Academy of Sciences (CAS), China

REVIEWED BY
Ming Shen,
Chinese Academy of Sciences (CAS), China
Emanuele Ciancia,
National Research Council (CNR), Italy
Yongquan Wang,
Shenzhen University, China

*CORRESPONDENCE
Ximena Aguilar Vega,
x.a.aguilar.vega@stir.ac.uk

RECEIVED 11 September 2025
REVISED 29 October 2025
ACCEPTED 10 November 2025
PUBLISHED 12 January 2026

CITATION
Aguilar Vega X, Jiang D, Fransson A, Chierici M, Iriarte JL, Kristoffersen A, Cárdenas C and Spyrakos E (2026) Coloured dissolved organic matter in a coastal arctic environment and the implications for dissolved organic carbon monitoring from Sentinel-2 MSI. *Front. Remote Sens.* 6:1703604. doi: 10.3389/frsen.2025.1703604



# Coloured dissolved organic matter in a coastal arctic environment and the implications for dissolved organic carbon monitoring from Sentinel-2 MSI

Ximena Aguilar Vega[1]*, Dalin Jiang[1], Agneta Fransson[2], Melissa Chierici[3], Jose Luis Iriarte[4], Arne Kristoffersen[5], Carlos Cárdenas[6] and Evangelos Spyrakos[1]

[1]Biological and Environmental Sciences, Faculty of Natural Sciences, University of Stirling, Stirling, United Kingdom, [2]Norwegian Polar Institute, Fram Centre, Tromsø, Norway, [3]Institute of Marine Research, Oceanography and Climate, Tromsø, Norway, [4]Universidad Austral de Chile, Puerto Montt, Chile, [5]Department of Physics and Technology, University of Bergen, Bergen, Norway, [6]Universidad de Magallanes, Punta Arenas, Chile

This study presents a rare, high-quality dataset of bio-geo-optical properties from an Arctic glacio-marine fjord (Kongsfjorden, Svalbard), collected during the critical spring melt and sea-ice transition period (April 2023). To our knowledge, this is the first study to utilise Sentinel-2 MSI to retrieve coloured dissolved organic matter (CDOM) and DOC in such an optically complex, high-latitude nearshore ecosystem during this season. Our findings directly address persistent challenges in Arctic remote sensing (RS). We first characterised the system's bio-geo-optical properties, identifying CDOM as the primary light-absorbing constituent. We then demonstrated that existing atmospheric correction models (ACOLITE, C2RCC, POLYMER) perform poorly over this area, showing large errors. To overcome this, we established a regionally tuned empirical algorithm using Sentinel-2 MSI Rrs bands (490, 560, 665, and 704 nm) that provides accurate estimations of CDOM absorption ($a_{CDOM}$ (443)) from both *in-situ* and MSI data. Furthermore, we established new relationships between CDOM and DOC using our *in-situ* data. Applying these to MSI imagery revealed spatio-temporal dynamics: higher DOC concentrations characterised the outer fjord in spring, contrasting with higher concentrations observed at the inner-fjord glacial terminus in summer. This contribution provides a validated methodology and crucial recommendations for the RS of carbon in optically complex Arctic nearshore environments.

KEYWORDS

**coloured dissolved organic matter, dissolved organic carbon, bio-optics, Sentinel-2 MSI, Svalbard, Kongsfjorden**

## 1 Introduction

The Arctic Ocean experiences an unusually high number of rivers and glacial discharges, a trend that could be exacerbated by climate warming (Feng et al., 2021; Peterson et al., 2002). This influx of organic-rich freshwater runoff results in Arctic surface waters being enriched with dissolved organic matter (DOM) and coloured dissolved organic

matter (CDOM) (Amon et al., 2024; Opsahl et al., 1999; Stedmon et al., 2011). Ice-derived organic carbon fluxes via glacial, sea-ice and icebergs meltwater are relatively small globally (6.3 Tg C $yr^{-1}$) (Wadham et al., 2019) but highly bioavailable and important for high latitude blue carbon (Chifflard et al., 2019). There are substantial uncertainties in carbon fluxes estimates and downstream impacts due to the very limited number of observations (Bruhwiler et al., 2021).

Light plays an essential role in glaciated coastal systems. Its interaction with ice, water, dissolved and particulate material influences many biogeochemical processes in marine systems (Castellani et al., 2022; Sandven et al., 2025). Variations in this interaction contain quantitative information about the physical and bio-geo-chemical properties of glaciated marine systems which could be used in Remote Sensing (RS) applications. RS offers an attractive solution for systematic monitoring of glaciated coastal systems, which are generally geographically remote, harsh and data-scarce environments (Jamal et al., 2025; Vitousek et al., 2023). RS approaches also allow observation at interannual scales, enabling the understanding of intricate variability and feedback mechanisms triggered by climate change (Zibordi et al., 2025). As sunlight permeates the water column, it undergoes alteration due to interactions with water molecules and optically active components, including phytoplankton, non-algal particles (NAP) such as detritus and minerals, and CDOM (Kirk, 1975). These modify the photon flux penetrating the ocean's surface layers, leading to absorption and scattering across various wavelengths, thereby altering the water's colour.

RS has provided critical insights into Earth's surface processes, but satellite sensors often lack the spectral and spatial resolution needed to resolve key features of organic carbon (Fichot et al., 2023). Gabarró et al. (2023) emphasized in their review the lack of RS-based CDOM products at high resolution in polar regions. They suggested, among others, the exploitation and improvements of Sentinel-2 sensors capabilities. While Sentinel-2 MultiSpectral Instrument (MSI) was initially designed with terrestrial mission objectives in mind, its radiometric and spatial resolutions offer a great opportunity for coastal applications especially at the land-marine continuum (Fichot et al., 2023). Several studies have explored the use of RS data for CDOM estimation in inland and coastal waters reaching diverse conclusions (Brezonik et al., 2015; Ficek et al., 2011; Liu et al., 2021; Mabit et al., 2022; Shanmugam, 2011; Tiwari and Shanmugam, 2011). It is considered that uncertainties in atmospheric correction (AC), the optical complexity of coastal waters and MSI signal to noise ratio over turbid waters affect the accuracy of CDOM retrievals (Renosh et al., 2020). Performance of AC algorithms over inland and coastal waters seem to vary across the different MSI bands with generally greater errors in red to NIR bands (Warren et al., 2019).

Polar coastal areas often exhibit unique optical characteristics due to the presence of ice, snow, and water (Irrgang et al., 2022). Monitoring near-shore Arctic systems from satellite sensors can be challenged by the high optical complexity of the water and high uncertainties in atmospheric correction (AC) (Comiso, 1991; Comiso, 2015; Klein et al., 2021). In polar regions, the atmosphere and surface conditions can differ significantly from other areas (Turner and Overland, 2009). For example, low sun angles, snow and ice cover (e.g., strong adjacency effects due to their high albedo), and unique atmospheric conditions may affect the accuracy of AC algorithms. Several methods have been developed depending on the characteristics of distinct marine and oceanic waters (Smith et al., 2019). Over open ocean waters, the black pixel assumption the ocean being totally absorbent is valid in the Near-InfraRed (NIR), whereas in coastal or turbid waters the latter is often not valid making the AC over these waters more challenging (Pahlevan et al., 2019). Glukhovets et al. (2022) reported that uncertainties in $a_{CDOM}$ retrievals were an order of magnitude higher than algorithmic error estimates, mainly due to unsatisfactory AC under Arctic conditions. Several studies (e.g., Gonçalves-Araujo et al., 2018; Juhls et al., 2019) report the need for improved AC tailored to the Arctic, as standard global approaches often fail in the presence of high CDOM, ice, and low illumination. Juhls et al. (2019) and Juhls et al. (2022) emphasize the importance of developing and validating region-specific DOC-CDOM relationships and algorithm parameterisations. Nevertheless, there is a sparsity of high quality polar nearshore radiometric measurements that are vital for validation and development of RS products (Lucas et al., 2023). Permafrost thaw and meltwater discharge introduce strong spatial and temporal variability, as reported in several studies (e.g., Hop and Wiencke, 2019) in addition to the short open-water period and rapid changes during spring snowmelt flood or ice break-up, limiting the temporal window for effective monitoring and validation (Herrault et al., 2016).

One of the most challenging aspects of developing robust, global ocean colour algorithms for DOC is that the relationship between DOC and CDOM is highly variable, and in some cases negatively correlated as has been shown, for example, in the Southern Ocean (Aurin et al., 2018; Vantrepotte et al., 2015). Concentration of CDOM does not co-vary with chlorophyll-*a* in Arctic waters, meaning that the majority of CDOM is not a phytoplankton degradation product but is imported from land (Clark et al., 2022; Efimova et al., 2023). Matsuoka et al. (2015) identified that variations in the spectral slope of CDOM absorption ($S_{CDOM}$) in the Arctic were partly explained by bacterial production and bacterial abundance variations.

Several approaches have been developed for retrieving water parameters such as CDOM from RS data, which can be grouped into three main types (Tyler et al., 2016). The first includes empirical algorithms, which rely on statistical relationships derived from the water-leaving signal. A key characteristic of empirical models is their reliance on *in situ* data for calibration, as the statistical relationships are likely to change between regions, seasons, or RS missions. While this makes them highly site-specific, empirical methods are straightforward to implement (e.g., Mannino et al., 2008; Shanmugam, 2011; Tiwari and Shanmugam, 2011; Ficek et al., 2011; Brezonik et al., 2015; Liu et al., 2021). For example, Nguyen et al. (2024) developed the *AquaCDOM* algorithm to estimate CDOM absorption at 412 nm from Rrs. They used band ratios to make it less sensitive to AC errors, allowing for consistent $a_{CDOM}$ (412) retrieval across different sensors (e.g., OLI and MSI).

The second type refers to analytical and semi-analytical models which utilize IOPs and AOPs inversion techniques to model the water's reflectance. Physical relationships are derived between the water parameters, the underwater light field, and the RS radiance. This method involves bio-optical and radiative transfer models to simulate light propagation and de-convolve the signal, determining each parameter's contribution to the total reflection. In the high

north, Gonçalves-Araujo et al. (2018) applied a modified version of the Garver-Siegel-Maritorena (GSM) algorithm in the western Arctic Ocean. They demonstrated that in these optically complex with high-CDOM, only a semi-analytical model could reliably separate the water's components and quantify $a_{CDOM}$ with low uncertainty. Similarly, Matsuoka et al. (2013) developed a semi-analytical algorithm for the southern Beaufort Sea that inverts MODIS reflectance to find $a_{CDOM}$.

Third, Machine learning approaches, which typically require large training datasets. Machine Learning applications like non-linear Neural Networks (NN) and Support Vector Machines (SVM) are powerful because they can capture both linear and complex non-linear relationships, giving them an advantage over conventional statistical approaches. A clear example of this approach is a study by Sun et al. (2021) were they trained and compared four different machine learning algorithms to retrieve $a_{CDOM}$ (254) from Landsat 8 imagery. The models were trained on a dataset of over 1,700 *in situ* measurements from inland waters covering a wide range of optically complex waters. All models achieved high accuracy ($R^2 > 0.70$), significantly outperforming traditional empirical models ($R^2 < 0.56$).

Empirical algorithms allow for regional re-tuning based on remote sensing reflectance and local constituent concentrations and tend to be less sensitive to AC uncertainties (e.g., Pahlevan et al., 2021). This contrasts with physics-based and machine learning models, which typically demand significantly larger datasets of IOPs or training data, respectively. Our contribution is providing a rare, high-quality dataset of bio-geo-optical properties of nearshore Arctic waters. Even though several published works have demonstrated that Sentinel-2 MSI can retrieve CDOM/DOC in inland (Cao et al., 2024) and riverine systems (El Kassar et al., 2023), including one pan-Arctic rivers study during ice-free conditions (Huang et al., 2019), and Arctic-specific evaluations of Sentinel-2 AC and nearshore optical retrievals (König et al., 2019; Klein et al., 2021).To our knowledge, this is the first study utilising Sentinel-2 MSI to retrieve CDOM/DOC in an Arctic nearshore marine ecosystem during the spring (melt/ice-transition) season.

Given the lack of studies on CDOM retrieval from Sentinel-2 MSI in the Arctic, the objective of this paper is not an exhaustive benchmark of all available CDOM algorithms. Rather, our aim is to demonstrate the feasibility of CDOM retrieval from Sentinel-2 MSI in nearshore Arctic waters by testing a set of algorithms with representative empirical formulations and band combinations. In this study, we characterised the optical properties of Kongsfjorden improving our understanding of its underwater light climate, evaluated the AC performance of Sentinel-2 MSI imagery, and proposed a method to estimate CDOM and its relationship with DOC. The aim of this study is to support improved CDOM and carbon monitoring of nearshore Arctic ecosystems through more accurate satellite-derived information.

# 2 Materials and methods

## 2.1 Study area

Fieldwork was carried out in Kongsfjorden between April 20th and 30th, 2023. Kongsfjorden is located on the western coast of Spitsbergen and spans roughly 25 km in length and between 5 and 10 km in width (Svendsen et al., 2002). The fjord is characterized by extensive glacial coverage, with around 80% of its drainage basin blanketed by ice (Kohler et al., 2007). Its dynamics are heavily influenced by tidewater glaciers, including Kronebreen and Kongsvegen at the fjord's head, as well as Conwaybreen and Blomstrandbreen situated along its northeastern and northern shores. Among these, Kongsvegen and Kronebreen stand out due to their significant ice fluxes (Schuler et al., 2020), with Kronebreen being particularly notable as one of Svalbard's most active calving glaciers (Holmes et al., 2023; Sevestre et al., 2015). Kongsfjorden maintains a hydrological connection to the North Atlantic via the Kongsfjordenrenna, which facilitates the inflow of warm Atlantic water from the West Spitsbergen Current. This inflow moderates the formation of winter sea ice. The Atlantic water typically enters along the southern fjord coast, where it mixes with meltwater and glacial runoff before exiting through the northern side, partly via Krossfjorden. The broad fjord entrance and its link to Krossfjorden allow oceanic swells generated by storms to propagate into the central fjord region (Cottier et al., 2005; Svendsen et al., 2002; Tverberg et al., 2019). Trophic conditions in Kongsfjorden in spring are characterised by low ratios between POC/N (POC/PON = 5.9–6.5), suggesting a high concentration of algal cells in the euphotic zone. In terms of optical conditions, suspended particles and sea-ice strongly affect the underwater light regime in the inner part of the fjord. For example, during the ice-free season (summer), the influence of suspended particles limits the extension of the euphotic zone to around 0.3 m in the innermost part of the fjord, while in the mid and outer parts can vart from 6 m to 30 m in winter (Svendsen et al., 2002).

## 2.2 Seawater sampling

Water sampling took place aboard the M/S Teisten along a transect of five stations (Figure 1). These stations extended from areas near sea ice (KBC) and glacier fronts (KB5G) to the mid- (KB3/4, KB4) and closer to the outer part (KB3) of Kongsfjorden, as well as across additional transects within the fjord. At each station, vertical profiles of salinity and temperature were collected from the surface to the bottom of the water column using a conductivity-temperature-pressure (CTD) sensor (SAIV). A total of 16 water samples were collected at varying depths of the water column using a single Niskin bottle deployed on a wire.

## 2.3 CDOM, DOC and TPC analyses

For CDOM absorption analysis, water samples were filtered through 0.2 µm Whatman nucleopore membrane filters. For particulate total carbon (TPC) and DOC analyses, water samples were filtered through pre-combusted GF/F filters (450 °C for 5 h; pore size 0.7 µm). All samples were kept frozen at −20 °C until immediate analysis upon the return to the laboratory. CDOM absorbance was measured using a dual-beam spectrophotometer Cary 4000 UV-Vis with Milli-Q water serving as a reference. Spectral measurements were collected from 200 to 800 nm at intervals of 0.5 nm. Absorbance ($A(\lambda)$) were transformed to CDOM absorption coefficients, $a_{CDOM}$ ($\lambda$) ($m^{-1}$), according to Coble (2007):

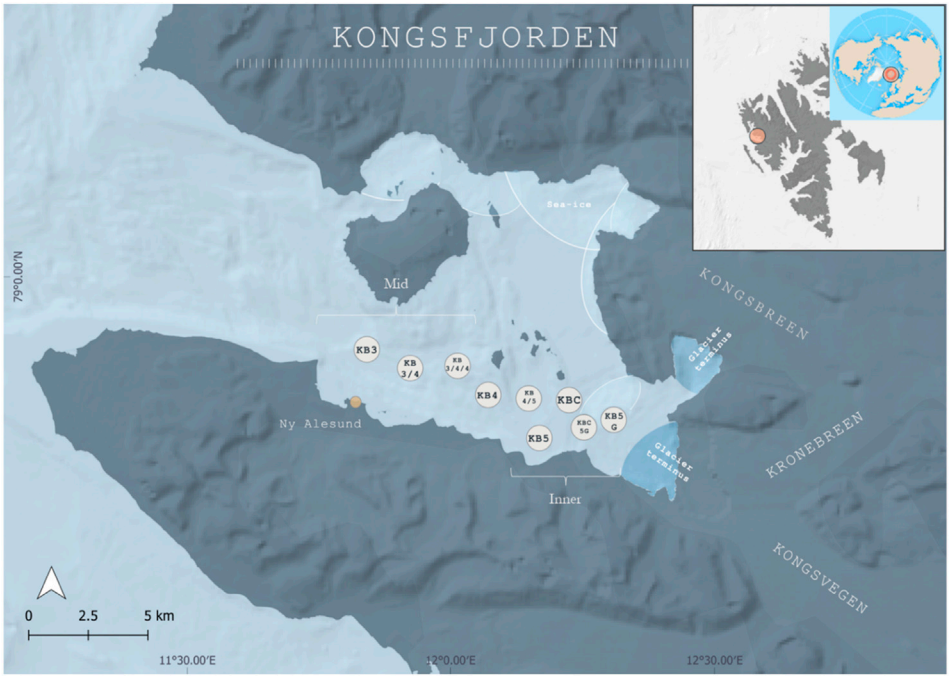


FIGURE 1
Study area map. Sampling stations are indicated by a white circle. Elevation data is sourced from Natural Earth, large scale data, 1:10 m.

$$a_{CDOM}(\lambda) = 2.303 * A(\lambda)/L$$

where 2.303 is the natural logarithm of 10, $A(\lambda)$ is the corrected spectrophotometer absorbance reading at a specific wavelength (λ), and $L$ is the path length of optical cell in meters (here 0.1 m).

## 2.4 Particle absorption (PABs)

Water collected from the Niskin bottle was filtered through Whatman GF/F filters (0.7 μm pore size). Filtration was done after water collection, and the filters were stored at −80 °C. A quantitative filter technique was used to measure the optical density of the filters based on placing filters inside an integrating sphere (Kishino et al., 1985; Stramski et al., 2015).

$$a_{p(\lambda)} = \left(OD_S(\lambda) - OD_{ref}(\lambda)\right)^* A \big/ (V\beta)$$

where $OD_S(\lambda)$ is the measured optical density of the specific sample, corrected for any stray light or nonlinearity effects, and $OD_{\mathrm{ref}}(\lambda)$ is the corresponding reference optical density measured using a wet blank filter. Furthermore, $A(\mathrm{m}^2)$ is the filter patch area and $V(\mathrm{m}^3)$ is the volume of the filtered water. The path length amplification factor$1/\beta$ is technically defined as the ratio between the optical and geometrical path length in the measurement set-up, but operationally it describes all contributions of scattering to the measured signal in the absorption meter. After measuring $a_{\mathrm{p}}(\lambda)$, the filters were bleached using a 1% sodium hypochlorite (NaClO) for 1h, and then the bleach was removed with a $H_2O_2$ solution. The measured optical density yields the NAP absorption ($a_{\mathrm{NAP}}(\lambda)$) using Equation 1. Finally, $a_{\mathrm{Phy}}(\lambda)$ was calculated by subtracting $a_{\mathrm{NAP}}(\lambda)$ from $a_{\mathrm{p}}(\lambda)$.

## 2.5 Underwater radiometry

Two USSIMO (*In-situ* marine optics) submersible hyperspectral radiometers were deployed to measure spectral upwelling radiance ($L_u^{0-}$) and downwelling irradiance ($E_d^{0-}$). $R_{\mathrm{rs}}(\lambda)$ (in $\mathrm{sr}^{-1}$) is defined here as the upwelling radiance emerging from the water column divided by the downwelling irradiance reaching the water surface using Equation 2. For calculating $R_{\mathrm{rs}}$ we considered a depth interval between 0 and 10 m depth.

$$R_{rs}^{0-} = L_u^{0-}/E_d^{0-} \quad (1)$$

Sub-surface $R_{\mathrm{rs}}(0^-)$ was converted to the above-water remote-sensing reflectance $R_{\mathrm{rs}}(0^+)$ to account for the bi-directional effects of the air-sea interface. This transfer was calculated using air-sea interface transfer equation from Lee et al. (2002):

$$R_{rs}(0^+) = \frac{0.52 \cdot R_{rs}(0^-)}{1 - 1.7 \cdot R_{rs}(0^-)} \quad (2)$$

where Rrs $(0^+)$ is the above-water remote-sensing reflectance and Rrs $(0^-)$ is the sub-surface remote-sensing reflectance (units: $\mathrm{sr}^{-1}$). And 0.52 and 1.7 are empirical constants derived from radiative transfer simulations that relate the sub-surface quantity to the above-water quantity.

Multispectral data at MSI bands were simulated from hyperspectral data through spectral convolution. This involved

TABLE 1 $a_{CDOM}$ algorithms and their input bands tested using the *in-situ* hyperspectral $R_{rs}$.

| Algorithm | $a_{CDOM}$ ($m^{-1}$) | Equation |
|---|---|---|
| Shanmugam (2011) | 350 | $a_{CDOM}(350) = 0.5567 \times \left(\frac{R_{rs}(443)}{R_{rs}(560)}\right)^{-2.0421}$ |
| Liu et al. (2021) | 350 | $a_{CDOM}(350) = 0.6503 \times \left(\frac{R_{rs}(665)}{R_{rs}(490)}\right) + 0.2334 \times \frac{R_{rs}(560)}{R_{rs}(490)} + 0.00529$ |
| Shanmugam (2011) | 412 | $a_{CDOM}(412) = 0.1866 \times \left(\frac{R_{rs}(443)}{R_{rs}(560)}\right)^{-1.9668}$ |
| Ficek et al. (2011) | 440 | $a_{CDOM}(440) = 3.65[R_{rs}(560)/R_{rs}(665)]^{-1.93}$ |
| Brezonik et al. (2015) | 440 | $a_{CDOM}(440) = \exp[2.038 - 0.832 \times \ln\left(\frac{R_{rs}(510)}{R_{rs}(754)}\right)]$ |
| Shanmugam (2011) | 440 | $a_{CDOM}(440) = a_{CDOM}(350) \cdot e^{(-S(440-350)-\gamma^0)}$<br>$\gamma^0 = \frac{a_{CDOM}(350) - (1/\gamma)}{a_{CDOM}(350)+(1/\gamma)}$<br>$S = 0.0058 \times \left(\frac{a_{CDOM}(412)}{a_{CDOM}(350)}\right)^{-0.9677}$<br>$\gamma = 2.9332 \times \left(\frac{a_{CDOM}(412)}{a_{CDOM}(350)}\right)^{-0.7506}$ |
| Mannino et al. (2008) | 443 | $a_{CDOM}(443) = \exp[-3.379 - 1.1513 \cdot \ln(R_{rs}(443))1.006 \cdot \ln(R_{rs}(560))]$ |
| Tiwari and Shanmugam et al. (2011) | 443 | $a_{CDOM}(443) = 0.00129 + 0.6543 \times \frac{R_{rs}(665)}{R_{rs}(490)}$ |

multiplying the hyperspectral data $L_u(\lambda)$ by the multispectral band SRF $SB(\lambda)$, integrating the result over all wavelength in the band ($\int \lambda \in B d\lambda$), and normalizing by the effective bandwidth in practice (Burggraaff, 2020).

## 2.6 Satellite data processing

We evaluated Sentinel-2 MSI imagery for mapping $a_{CDOM}$ across the study area. MSI records 13 spectral bands (443–2,190 nm) at 10–60 m resolution at nadir. Level-1C (top-of-atmosphere, georeferenced) scenes were downloaded from the Copernicus Open Access Hub. Two S-2 MSI images matched up with the *in-situ* data. We followed the widely accepted time difference of +/−1 for satellite-in situ matchups in coastal studies (e.g., +/− 30 h in Warren et al., 2019; Pahlevan et al., 2021). These images were used to evaluate the performance of different atmospheric corrections against the *in-situ* $R_{rs}$. A total of six S-2 MSI images were processed to demonstrate the application of our CDOM, DOC estimation models during a typical for the area melt season (May–August). All S-2 MSI images were resampled to 20 × 20 m resolution and then subset to the area covering Krossfjorden. Idepix was applied to S-2 MSI images to mask pixels identified as cloud, cloud_ambiguous, cloud_sure, cloud_buffer, cloud_shadow, cirrus_sure, cirrus_ambiguous, and invalid. Areas of wet-snow and ice patches were identified visually and were masked using hand-digitised polygons. The median S-2 MSI $R_{rs}$ value was calculated from a 3 × 3 window, and they were compared with the *in-situ* radiometric data to evaluate atmospheric correction models and used to develop CDOM estimation algorithms. We considered three atmospheric correction models, used with their respective default settings: C2RCC, ACOLITE v20231023 (Hieronymi et al., 2023), and POLYMER v4.16 (Steinmetz and Ramon, 2018), that have shown applicability to nearshore marine waters (Warren et al., 2019).

## 2.7 $a_{CDOM}$ and DOC algorithms

We tested eight existing community-established $a_{CDOM}$ algorithms for inland, transitional or coastal waters (Table 1). All algorithms were firstly tested using the *in-situ* hyperspectral $R_{rs}$ and $a_{CDOM}$ measurements. The best-performing algorithm formulations were then tuned against the *in-situ* hyperspectral $R_{rs}$, and the tuned algorithm was furtherly tested using the MSI $R_{rs}$ from the best-performing AC model. The $a_{CDOM}$ and DOC relationship was modelled using all available *in-situ* data ($n$ = 25).

Performance was assessed using the following statistics:

$$R^2 = \left(\Sigma\left((x_i - \bar{x})(y_i - \bar{y})\right) \Big/ \left(\sqrt{(\Sigma (x_i - \bar{x})^2)}\sqrt{(\Sigma (y_i - \bar{y})^2)}\right)\right)^2$$

Root mean square error (RMSE):

$$RMSE = \sqrt{\left((1/n) * \Sigma (x_i - y_i)^2\right)}$$

Mean absolute percentage error (MAPE):

$$MAPE = (100/n) * \Sigma \left|(x_i - y_i)/x_i\right|$$

Median symmetric accuracy (MdSA)

$$\text{MdSA} = 100\left(\exp\left(\text{M}\left|\log_e\left(\frac{y_i}{x_i}\right)\right|\right) - 1\right)$$

Symmetric signed percentage bias (SSPB)

$$\text{SSPB} = 100\left(sgn\left(M\log_e\left(\frac{y_i}{x_i}\right)\right)\left(\exp\left(\left|M\log_e\left(\frac{y_i}{x_i}\right)\right|\right) - 1\right)\right)$$

Mean Spectral Reflectance Difference (MSRD)

$$\text{MSRD} = \frac{1}{n}\sum_{i=1}^{n}\left|R_{rs,i}(\lambda) - R_{rs,j}(\lambda)\right|$$

where, $x_i$ and $y_i$ are the estimated (or satellite-derived) and *in-situ* data, respectively. $\bar{x}$ and $\bar{y}$ are the mean values, respectively, and $n$ is the number of data pairs.

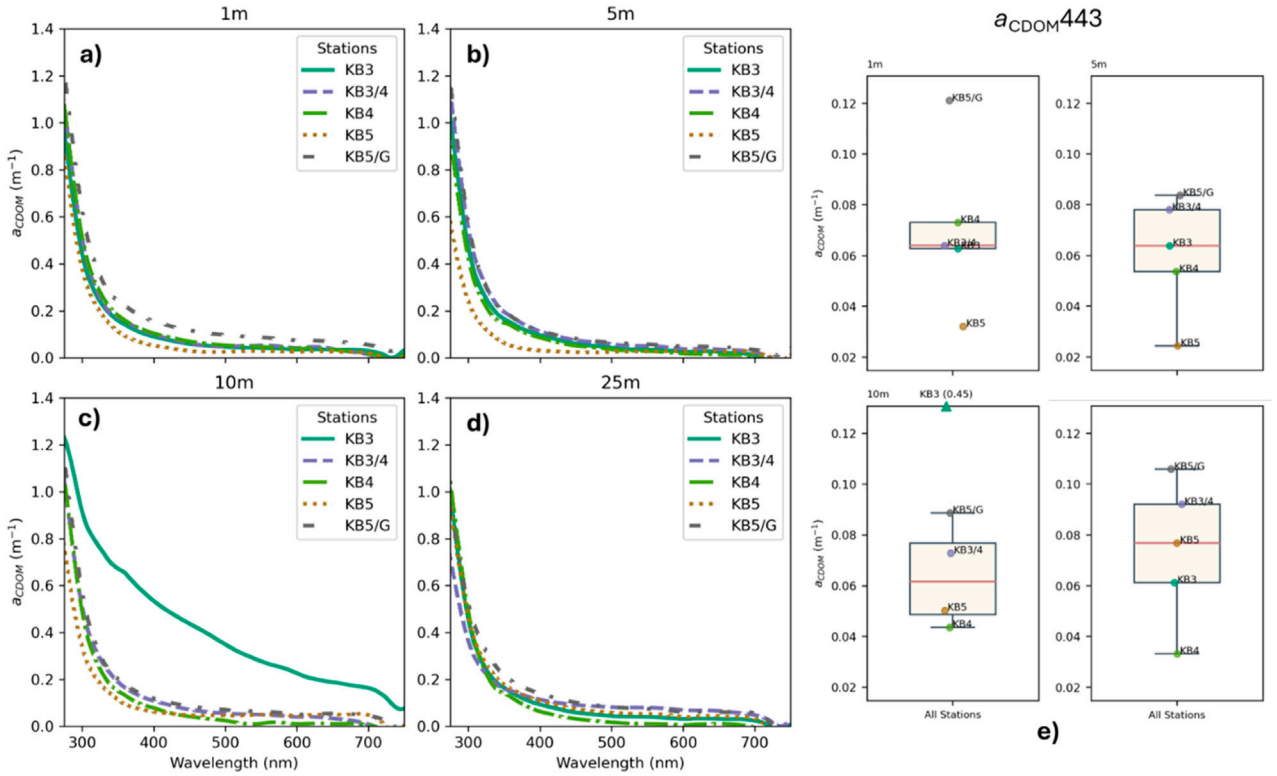


FIGURE 2
Marine water $a_{CDOM}$ spectra **(a–d)**, and $a_{CDOM}$ (443) boxplots **(e)**, for all stations and depths.

# 3 Results

## 3.1 Bio-geo-optical characterisation of Kongsfjorden waters

### 3.1.1 Coloured dissolved organic matter

We found that $a_{CDOM}$ (443) ranged between 0.024 and 0.445 $m^{-1}$ across all depths and stations (Figures 2a-d), with a mean value of 0.087 ± 0.085 $m^{-1}$. Station KB3 showed a marked subsurface high $a_{CDOM}$ (443) value of 0.445 $m^{-1}$ at 10 m (light blue solid line in Figures 2c,e). KB3/4 and KB4 displayed relatively lower $a_{CDOM}$ values across all depths. At 1 m, $a_{CDOM}$ (443) nm was consistent across most stations, with the notable exceptions of a high-value outlier at station KB5/G and a low-value outlier at station KB5. In contrast to the surface layer, 5 m depth exhibited greater heterogeneity in $a_{CDOM}$ (443), with values distributed across a wider range and no distinct statistical outliers. While most stations at 10 m showed $a_{CDOM}$ (443) values consistent with the 5 m layer, the overall distribution was heavily influenced by KB3 which was more than five times higher (0.45 $m^{-1}$) than any other station in the transect (Figure 2e). At 25 m $a_{CDOM}$ (443) was highest and most variable, with the largest interquartile range observed across the entire water column. While station KB3 exhibited the single highest $a_{CDOM}$ (443) in the entire dataset at 10 m, station KB5/G consistently recorded the highest values at all other depths (1, 5, and 25 m).

### 3.1.2 Absorption budgets

Ternary plots of five wavelengths (443, 490, 560, 665, and 704 nm) were used to examine the relative contributions of $a_{CDOM}$, non-algal particles ($a_{NAP}$), and phytoplankton pigments ($a_{Phy}$) to the absorption signal of Kongsfjorden waters (Figure 3). $a_{CDOM}$ constituted the principal contributor to total light absorption in Kongsfjorden (Figure 3). At the blue part of the electromagnetic spectrum (λ = 443 nm), $a_{CDOM}$ dominated (65%–90%) the absorption composition, with most samples clustering close to the CDOM apex. At 490 nm, $a_{CDOM}$ still dominated (60%–85%) the absorption signal, although the relative contribution of $a_{Phy}$ increased to 10%–30%, whereas $a_{NAP}$ remained negligible except in the glacier-plume sample at all wavelengths (K5G, 10 m). At 560 nm, the relative contribution of $a_{Phy}$ reached occasionally ~35%, reflecting the emergence of the pigment shoulder in this part of the spectrum. At the chlorophyll-a red absorption maximum (665 nm), $a_{Phy}$ contributions to absorption signal were comparable to that of $a_{CDOM}$, accounting for 25%–45% of the total absorption. At 704 nm, $a_{Phy}$ absorption significantly weakened, with $a_{CDOM}$ once again dominating, making up 65%–90% of the total absorption.

We observed distinct spatial and vertical patterns in the absorption budget. Waters near the glacier terminus (KB5G, 10 m) were dominated by mineral particles, with $a_{NAP}$ contributing over 70% across all wavelengths. The highest relative contributions of $a_{CDOM}$ (65%–90%) were observed at the inner-fjord

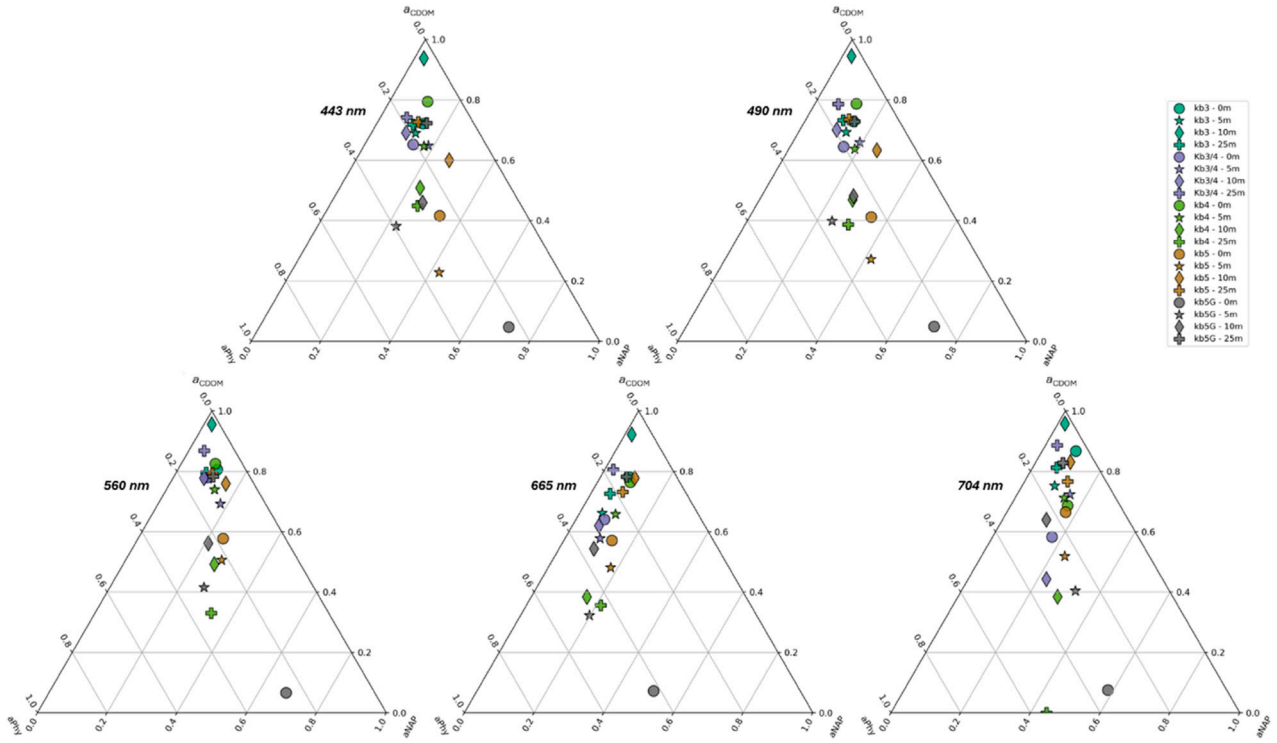


FIGURE 3
Relative contribution of $a_{CDOM}$, $a_{Phy}$ and $a_{NAP}$ to total absorption at five wavelengths in Kongsfjorden, Svalbard. Each symbol denotes a discrete water sample; colour/shape represents station and depth. Samples plot near an apex when that constituent contributes most of the absorption at the given wavelength. Note the $a_{CDOM}$ dominance in the blue (443–490 nm), the rise of $a_{Phy}$ contributions at the chlorophyll-a red peak (665 nm), and the unique $a_{NAP}$-rich sample (KB5G, 10 m).

stations (KB5G). In the mid-fjord (KB4), reduced turbidity allowed for modest phytoplankton development, which absorption was most evident between 560 and 665 nm. Closer to the mid part of the fjord (KB3), $a_{CDOM}$ contributions declined with depth, while $a_{Phy}$ recorded higher contributions especially at 10 m.

## 3.2 CDOM and organic carbon relationship

Initially, we tested published algorithms for deriving DOC from $a_{CDOM}$, but they yielded poor performance metrics with our dataset (e.g., Shen et al., 2016; Fichot and Benner, 2011). Subsequently, recalibrating these models with our *in-situ* data led to a considerable improvement in their accuracy (Table 2). Nevertheless, a simple linear regression model, developed directly from our data, ultimately outperformed the more complex algorithms and provided the best overall results. DOC showed positive correlations with $a_{CDOM}$ at all four wavelengths tested: 275, 330, 350, and 443 nm (Table 2). The strongest linear relationships were observed at 350 nm ($R^2$ = 0.80) and 443 nm ($R^2$ = 0.76), indicating that $a_{CDOM}$ at these wavelengths can serve as reliable proxies for DOC. Overall, $a_{CDOM}$ in the 330–443 nm range showed consistent and robust association with DOC, supporting its use in optical water quality assessments and biogeochemical studies in Kongsfjorden during spring.

## 3.3 *In-situ* $R_{rs}$ spectra and S-2 MSI atmospheric correction

*In-situ* $R_{rs}$ spectra (Figure 4a) showed variation in magnitude and shape. Surface spectra from Kongsfjorden exhibited peaks at around 500 nm or 560 nm followed by a steady decline towards the red part of the electromagnetic spectrum at most stations. Spectra from KB5, KB5G, KB3 and KB3/4/4 generally had lower mean reflectance and less pronounced peaks than the ones from the remaining stations. KB3/4 showed the highest $R_{rs}$ at longer wavelengths. Figures 4b–d show the $R_{rs}$ spectra processed through C2RCC, POLYMER, and ACOLITE atmospheric corrections respectively. C2RCC showed very little variability in their spectra magnitude and shape with higher $R_{rs}$ values in the blue that gradually decreased to almost negligible values at longer wavelengths. POLYMER spectra showed greater magnitude and shape variability, preserving the $R_{rs}$ peak at around 500 nm or 560 nm. ACOLITE results showed higher $R_{rs}$ values overall, particularly at shorter wavelengths (450–550 nm).

Table 3 presents the performance metrics for each atmospheric correction processor and MSI band. All processors produced generally large errors, with ACOLITE showing the lowest MAPE, MSRD, SSPB, and MSA across most bands. C2RCC had a lower number of valid pixels and showed the poorest performances compared to the other two AC models. Bias was found to be

TABLE 2 Statistical performance of models estimating DOC from $R_{rs}$.

| Linear regression | | | | | | | | | |
|---|---|---|---|---|---|---|---|---|---|
| wl of $a_{CDOM}$ | N | Slope | Intercept | $R^2$ | RMSE | MAPD% | SSPB% | MdSA% | MSRD |
| $a_{275}$ | 17 | 0.05 | 0.94 | 0.33 | 0.11 | 7.31 | 3.08 | 7.31 | 0.01 |
| $a_{330}$ | 17 | 0.07 | 0.16 | 0.78 | 0.06 | 14.77 | −4.09 | 17.33 | 0.06 |
| $a_{350}$ | 17 | 0.07 | 0.10 | 0.80 | 0.06 | 16.88 | −5.70 | 20.31 | 0.10 |
| $a_{443}$ | 17 | 0.05 | 0.02 | 0.76 | 0.05 | 35.39 | −13.54 | 44.08 | 0.49 |
| **Fitted DOC model** | | | | | | | | | |
| Ratio | N | A, coeff. | C1, coeff. | $R^2$ | RMSE | MAPD% | SSPB% | MdSA% | MSRD |
| a(330)/a(350) | 17 | 11.63 | −8.69 | 0.712 | 0.89 | 40.99 | −19.33 | 69.46 | 20.26 |
| a(275)/a(443) | 17 | 4.60 | −0.65 | 0.194 | 1.49 | 49.19 | −31.15 | 96.81 | 19.81 |
| a(330)/a(443) | 17 | 2.48 | −0.91 | 0.021 | 1.65 | 44.31 | −32.32 | 79.58 | 20.41 |
| a(350)/a(443) | 17 | 0.94 | −0.14 | −0.141 | 1.78 | 44.48 | −17.06 | 80.12 | 17.28 |
| **Previously published DOC models** | | | | | | | | | |
| wl of $a_{CDOM}$ | N | Model | | $R^2$ | RMSE | MAPD% | SSPB% | MdSA% | MSRD |
| $a_{275}$, $a_{330}$ | 17 | Shen et al. (2016) | | −798.46 | 47.07 | 5115.59 | 192.47 | 5115.59 | 59531.02 |
| $a_{275}$, $a_{330}$ | 17 | Fichot and Benner (2011) | | −1870.61 | 72.02 | 7850.40 | 195.03 | 7850.40 | 133658.53 |

The table compares key performance metrics for published algorithms, their locally recalibrated versions, and a simple linear regression developed in this study. All models were evaluated against *in-situ* DOC measurements.

negative across most bands, indicating that all AC processors tested mostly underestimated $R_{rs}$, when compared to *in-situ* data.

Figure 5 shows the scatterplots of the three AC models tested here against the *in-situ* $R_{rs}$ data at the sampling stations. ACOLITE overestimated $R_{rs}$ at 443 nm. It showed its lowest errors at 665 nm and 740 nm when compared to its performance across other parts of the electromagnetic spectrum. POLYMER demonstrated better performance in the blue-green part of the spectrum, but its errors were larger in the red region. $R_{rs}$ collected from station KB3/4/4 were closer to the 1:1 line for bands 430, 490, and 560 nm for all AC processors tested here. Match-up points from KB3/4 were found far from the 1:1 line for bands 665 and 704 nm across all AC processors.

## 3.4 CDOM estimation from *in situ* $R_{rs}$

We first benchmarked existing CDOM algorithms with their original parameterisations for $a_{CDOM}$ (443), using the *in-situ* $R_{rs}$ spectra and $a_{CDOM}$ values (Table 4). SHA11C model showed the lowest errors in the retrieval of CDOM MAPE 50.1%, MSRD 0.371 ($sr^{-1}$), SSP -15.89%, and MdSA 44.04%, among all algorithms tested. MAN08 was the second best, with MAPE 60%, MSRD 0.534 ($sr^{-1}$), SSPB -37.77, and MdSA 68.57%. The remaining CDOM algorithms tested using their original parameterisations showed poor results. These models exhibited MAPE greater than 126% and MSRD higher than 2.86 ($sr^{-1}$).

To tune the algorithms to our Kongsfjorden dataset, all algorithm formulations were computed from hyperspectral *in-situ* reflectance data to predict $a_{CDOM}$. We then fitted linear and power-law regression between the algorithms and the measured $a_{CDOM}$ (Figure 6). From these, top-performing algorithms were identified based on their performance metrics and the availability of bands in MSI. To develop an algorithm for satellite data, the LIU21 model structure was chosen because it showed the best performance when fitted with our data (Supplementary Appendix 7.1). The best performing model using the *in-situ* data $a_{CDOM}$ (443) was based on LIU21 and was expressed as:

$$a_{CDOM}KB = 0.3444 + 1.5765 \times \frac{R_{rs}(665)}{R_{rs}(490)} - 0.5018 \times \frac{R_{rs}(560)}{R_{rs}(490)} - 1.3805 \times \frac{R_{rs}(704)}{R_{rs}(490)}$$

The addition of the R704/R490 band ratio consistently improved model accuracy for estimating $a_{CDOM}$ (443). Multiple combinations of $R_{rs}$ band ratios were tested using linear regression models to find the best band ratio combination. This procedure is like empirical tuning approaches in previous studies (e.g., Matsuoka et al., 2013; Seegers et al., 2018), fitted to the available Sentinel-2 MSI bands. While 704 nm is not a primary wavelength for CDOM absorption, it may capture optical effects (e.g., scattering) that covary with CDOM concentrations in these waters (Figure 7).

## 3.5 CDOM from Sentinel-2 MSI

Separated linear models were recalibrated using *in situ* $a_{CDOM}$ (443) and Sentinel-2 MSI $R_{rs}$ data produced by each correction method (Figure 6). For ACOLITE, POLYMER, and C2RCC, new

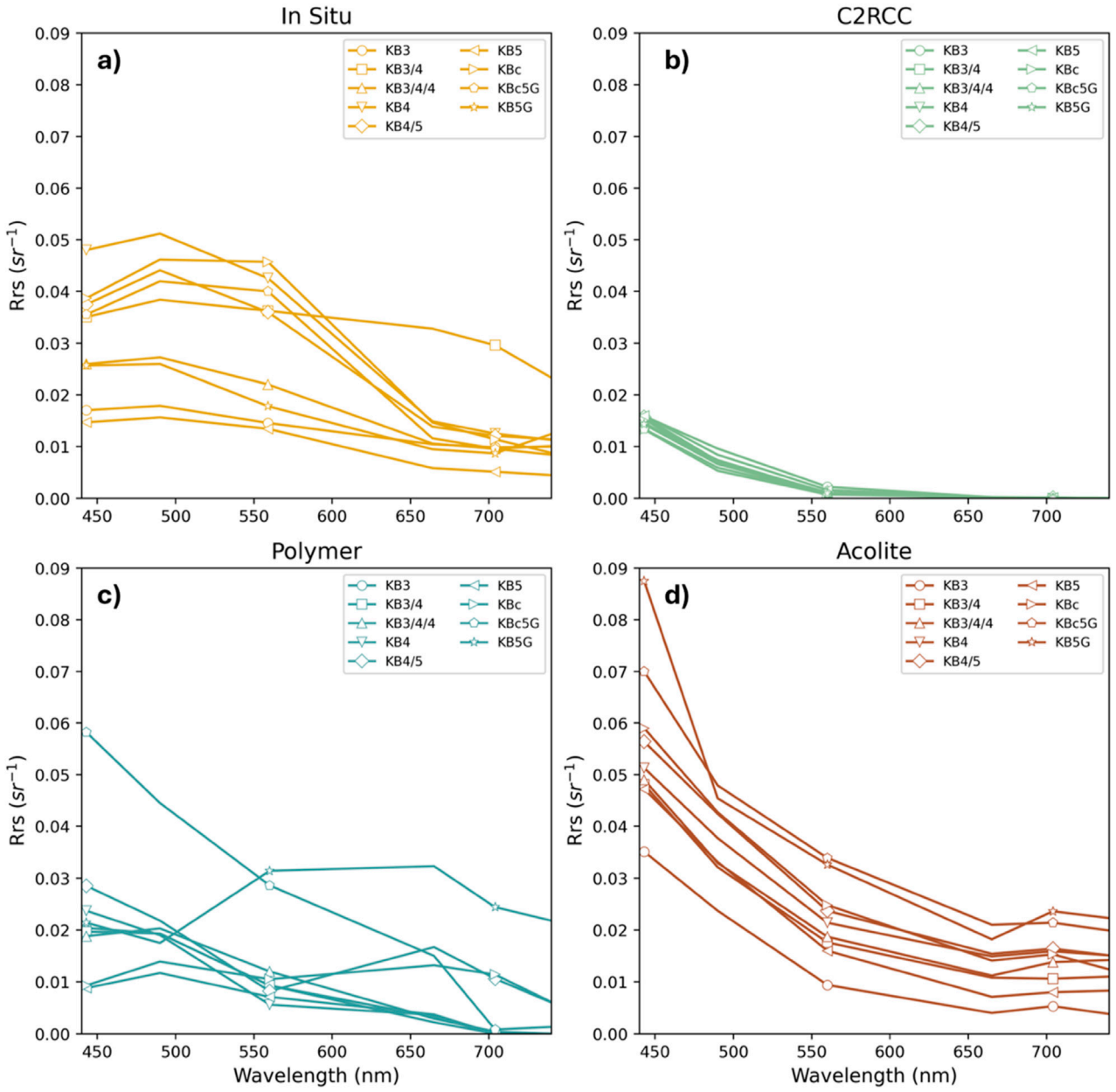


FIGURE 4
$R_{rs}$ spectra ($sr^{-1}$) from **(a)** *in-situ* measurements and three atmospheric correction algorithms: **(b)** C2RCC **(c)** POLYMER, and **(d)** ACOLITE. Each subplot displays spectral curves across wavelengths from 450 to 700 nm, for different sampling stations.

models were trained using the same reflectance ratios $R_{665}/R_{490}$, $R_{560}/R_{490}$, and $R_{704}/R_{490}$ and independently evaluated using performance metrics (Table 5). This correction-specific recalibration improved model fit. All models gave good results. The model based on POLYMER was the best performing $a_{CDOM}$ (443) algorithm (Table 5), with a very high $R^2$ of 0.990, low RMSE (0.00280 $m^{-1}$) and MAPE (3.48%), and almost zero bias. The models using C2RCC ($R^2$ = 0.964, RMSE = 0.00305 $m^{-1}$, MAPE = 3.09%, Bias = 0) and ACOLITE data ($R^2$ = 0.886, RMSE = 0.00968 $m^{-1}$, MAPE = 17.04%) also showed high $R^2$ and low errors.

In early spring (March–April), $a_{CDOM}$ (443) was spatially uniform at moderate concentrations throughout most of the fjord's surface, with some areas depicting low concentrations near the marine terminating glaciers (~0–0.06 $a_{CDOM}$ (443) $m^{-1}$) (Figures 8a,b). As the melt season progressed (May–August), background CDOM declined, but discrete, high-CDOM plumes started developing in front of marine-terminating glaciers (min = ~ 0.60, max = ~ 0.24 $a_{CDOM}$ (443) $m^{-1}$), producing a markedly patchier field with high $a_{CDOM}$ (443) relative to earlier months (Figures 8d–f). In general, a shift from Spring to Summer was clear: the fjord in Spring diluted $a_{CDOM}$ (443) signal by sea-ice and glacial meltwater, whereas glacial water in Summer acted as a supplier of $a_{CDOM}$ (443) (Figures 8d–f), being the 26th of August the day with the highest $a_{CDOM}$ (443) at the inner fjord in comparison to the others in this study.

TABLE 3 Performance metrics for each atmospheric correction processor and MSI band.

| AC processor | Band | N | MAPE (%) | MSRD ($sr^{-1}$) | SSPB (%) | MdSA (%) |
|---|---|---|---|---|---|---|
| POLYMER | 443 | 9 | 55.30 | 0.04 | −82.40 | 83.95 |
| | 490 | 9 | 61.88 | 0.04 | −92.76 | 89.76 |
| | 560 | 9 | 68.49 | 0.04 | −113.56 | 111.53 |
| | 665 | 9 | 68.18 | 0.02 | −91.53 | 99.32 |
| | 704 | 9 | 82.60 | 0.02 | −140.21 | 191.30 |
| | 740 | 9 | 81.30 | 0.02 | −153.38 | 200.00 |
| ACOLITE | 443 | 9 | 30.86 | 0.02 | 6.61 | 13.74 |
| | 490 | 9 | 33.23 | 0.03 | −38.99 | 38.86 |
| | 560 | 9 | 52.92 | 0.03 | −76.32 | 89.38 |
| | 665 | 9 | 41.28 | 0.02 | −59.24 | 56.41 |
| | 704 | 9 | 38.15 | 0.02 | −36.82 | 31.40 |
| | 740 | 9 | 28.36 | 0.01 | −38.64 | 25.35 |
| C2RCC | 443 | 8 | 68.51 | 0.04 | −107.51 | 122.11 |
| | 490 | 8 | 85.51 | 0.06 | −151.35 | 164.08 |
| | 560 | 8 | 96.95 | 0.06 | −188.39 | 193.34 |
| | 665 | 8 | 99.47 | 0.03 | −197.89 | 198.26 |
| | 704 | 8 | 99.75 | 0.03 | −199.00 | 200.00 |
| | 740 | 8 | 100.00 | 0.02 | −200.00 | 200.00 |

During early spring (March–May), DOC concentrations were generally higher in the outer fjord, while lower levels were observed near the marine-terminating glaciers (Figures 9a–c). As the melt season advanced (June–August), background DOC levels increased toward the inner fjord. High-DOC plumes appeared in areas influenced by the marine-terminating glaciers forming a distinct gradient: elevated DOC concentrations in the inner fjord, decreasing toward the outer regions (Figures 9d–f). In summary, the transition from spring to summer marked a shift in DOC dynamics: in spring, DOC appeared to be diluted across the fjord, likely due to inputs from sea-ice and glacial meltwater, while in summer, glacial meltwater became a primary source of DOC (Figures 9d–f).

# 4 Discussion

Our results show that CDOM was the primary contributor to light absorption along the fjord in Kongsfjorden, accounting for over 50% of the total absorption. This finding is consistent with previous research in Arctic coastal systems, where $a_{CDOM}$ typically constitutes 66%–76% of the total non-water absorption at 443 nm (e.g., Gonçalves-Araujo et al., 2016; Matsuoka et al., 2013). In this study, $a_{CDOM}$ (443) ranged from 0.024 to 0.445 $m^{-1}$. Notably, the highest values were observed both in oceanic-influenced waters (KB3, 10 m) and in surface waters near sea-ice and marine-terminating glaciers (KB5/G). This suggests that in glacio-marine systems, CDOM sources can be significant to both the marine and glacial endmembers of the fjord. The dominance of $a_{CDOM}$ persisted even in waters with high Chla fluorescence and extended into the red spectral region.

The contribution of $a_{Phy}$, however, varied significantly. While accounting for less than 30% of total absorption in the blue spectral region, its relative importance increased with wavelength, reaching ~40% at 665 nm. The overwhelming dominance of $a_{CDOM}$, especially in the blue-green spectral range, helps explain why standard empirical Chla algorithms often perform poorly in Arctic waters (e.g., Lewis et al., 2016; Zoffoli et al., 2025). Our absorption budget results suggest that Chla algorithms using blue-green or red-NIR bands are prone to overestimation in these nearshore waters unless they are specifically designed to account for the high and variable $a_{CDOM}$ background. Additionally, the presence of CDOM can change the water colour of well-known hues characterised by strong algal blooms as reported by Tessin et al. (2024) in Norwegian fjords, where they observed a coccolithophore bloom peak shift from 490 nm to 590 nm explained by an elevated CDOM absorption located at the algal bloom.

In glacial plume areas (inner fjord), the optical environment shifted dramatically in one station (KB5G, 10 m), with $a_{NAP}$ dominating the absorption signal (80%) near the land fast sea-ice and the glacier terminus. These findings align with other Arctic studies documenting the profound influence of freshwater inputs. For instance, Hill and Zimmerman (2016) found that sea-ice melt enriched surface waters with both CDOM and NAP. Additionally, stratified systems can trap low-particle meltwater in a surface lens, as observed by Mascarenhas and Zielinski (2019). Therefore, $R_{rs}$ in

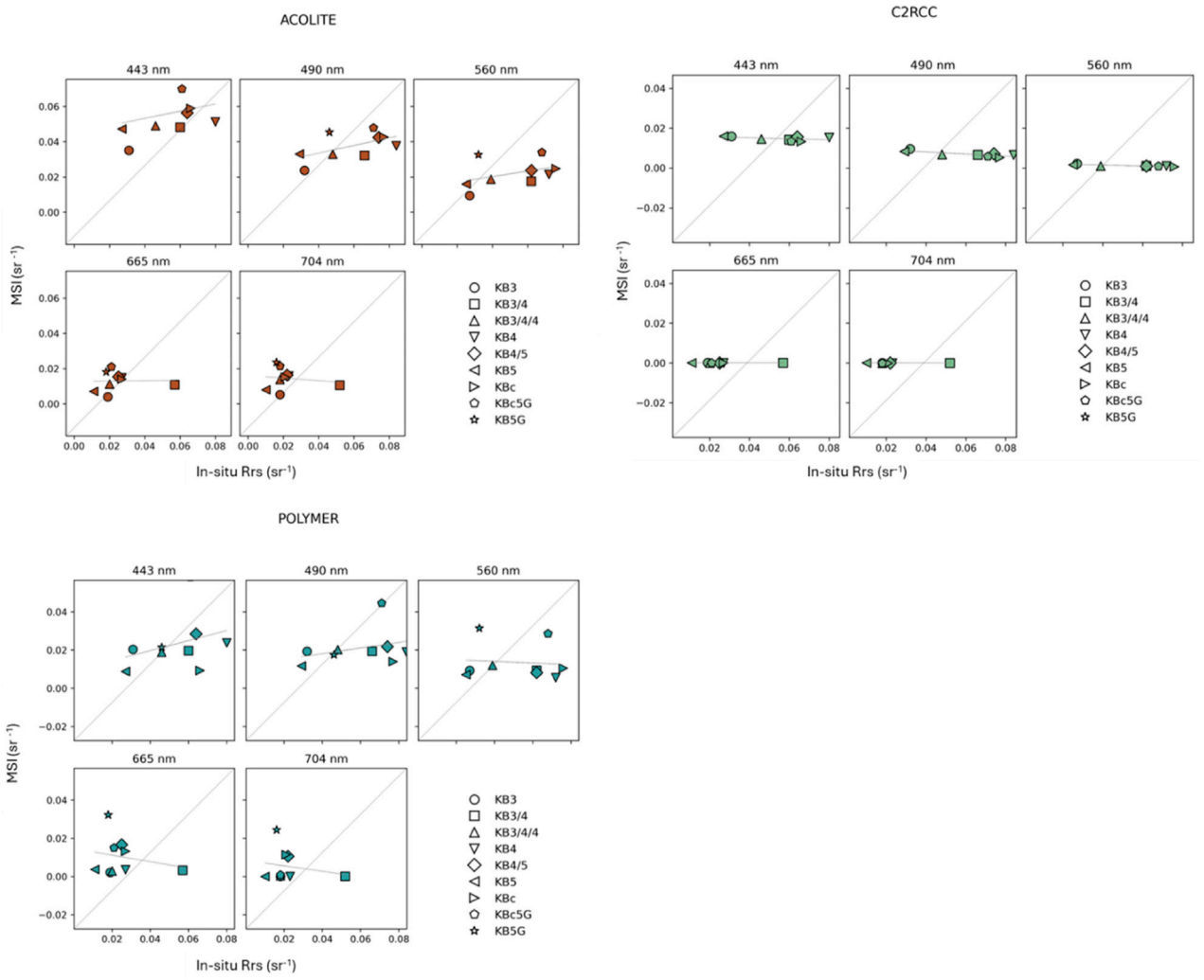


FIGURE 5
Scatterplots of the three AC models tested here against the *in-situ* $R_{rs}$ data at the sampling stations.

**TABLE 4** Performance metrics of the $a_{CDOM}$ retrieval algorithms tested using *in-situ* $R_{rs}$ spectra and $a_{CDOM}$ values.

| wl of $a_{CDOM}$ (nm) | Algorithm | $R^2$ | MAPE % | RMSE ($sr^{-1}$) | SSPB (%) | MdSA (%) |
|---|---|---|---|---|---|---|
| 350 | Shanmugam (2011) (SHA11A) | −67.30 | 205.60 | 6.84 | 137.02 | 137.02 |
| 350 | Liu et al. (2021) (LIU21) | −156.17 | 319.30 | 17.00 | 167.27 | 167.27 |
| 412 | Shanmugam (2011) (SHA11B) | −9.18 | 126.50 | 2.86 | 58.40 | 61.27 |
| 440 | Ficek et al. (2011) (FIC11) | −6663.12 | 3846.80 | 2844.32 | 3.28 | 29.45 |
| 440 | Brezonik et al. (2015) (BRE15) | −38443.62 | 9631.50 | 14253.69 | 6120.40 | 6120.40 |
| 440 | Shanmugam (2011) (SHA11C) | −0.922 | 50.1 | 0.371 | −15.89 | 44.04 |
| 443 | Mannino et al. (2008) (MAN08) | −1.43 | 60.10 | 0.534 | −37.77 | 68.57 |
| 443 | Tiwari and Shanmugam (2011) (T&S11) | −222.10 | 712.00 | 97.69 | 343.34 | 343.34 |

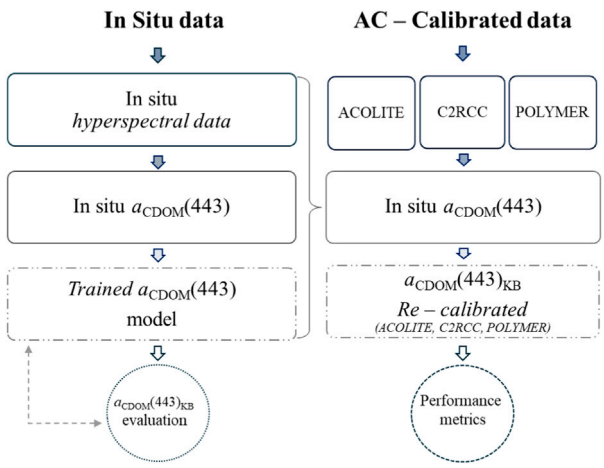


FIGURE 6
Calibration and validation phases for the tuned $a_{CDOM}(443)_{KB}$ algorithm.

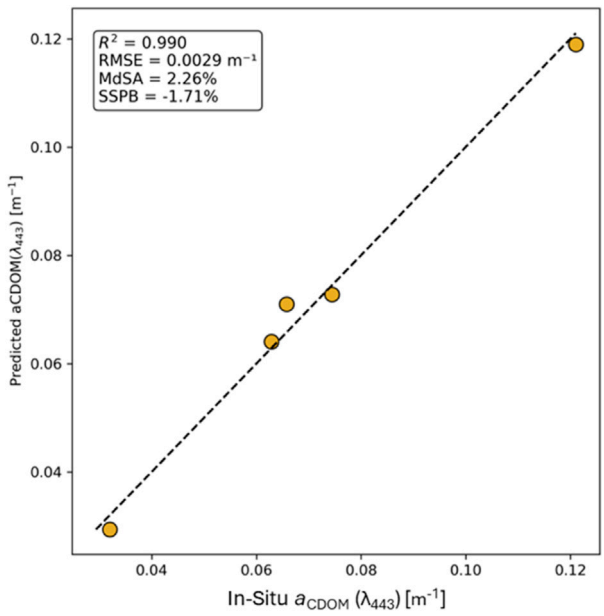


FIGURE 7
*In-situ* $a_{CDOM}$ (443) (x-axis) vs. predicted $a_{CDOM}$ (443) y-axis.

such turbid areas must account for both the strong absorption and the associated scattering effects of mineral particles to avoid substantial errors.

## 4.1 Implications for ocean colour remote sensing

Obtaining accurate water reflectance in high-latitude fjords is hampered by challenging factors. First, the water itself is optically contradictory: high CDOM concentrations darken the water by absorbing light in the blue-green wavelengths, while suspended glacial sediments simultaneously brighten it through intense scattering in the red and near-infrared (Zheng and DiGiacomo, 2017). Second, the low solar elevation angles prevailing at high latitudes force sunlight to travel through a longer atmospheric path. This amplifies the contribution of atmospheric haze and aerosols, making the atmospheric 'noise' much louder relative to the faint signal from the water and challenging the limits of standard AC models (Tessin et al., 2024). Third, adjacency effects from nearby sea-ice and snow-covered land, which normally present high reflectance, introduce a highly variable source of light contamination, which AC algorithms can misinterpret as atmospheric haze or in-water turbidity (König et al., 2019). Collectively, these factors create systematic errors that affect algorithms reliant on the 412–443 nm bands and can lead to uncertainties in $a_{CDOM}$ retrievals exceeding 100% in Northern seas (Glukhovets et al., 2021). Our study demonstrated that standard AC models (ACOLITE, C2RCC, POLYMER) performed poorly, which is consistent with the literature. Factors prevalent in the Arctic, such as low sun angles, pervasive cloud cover, adjacency effects from sea ice, and the extreme optical complexity of turbid, glacio-marine waters, are known to contribute to very high uncertainties in satellite-derived products (Juhls et al., 2022). For example, studies using sensors over similar waters have reported that real uncertainties in AC-derived products can exceed 100%, even when algorithm-predicted errors are estimated to be much lower, near 10% (Glukhovets et al., 2021).

The importance of mitigating these issues was evident in our results. In our study, ACOLITE provided more reliable results, especially at 665 and 704 nm. ACOLITE AC has been used in several inland and coastal studies and has shown promising results in turbid waters (Vanhellemont and Ruddick, 2018; Vanhellemont and Ruddick, 202; Zhang, et al., 2023). Warren et al. (2019) found that ACOLITE delivered higher $R^2$ in the red and NIR band in the inland waters and performed better in the red bands than in the NIR ones in coastal waters. König et al. (2019) tested several AC algorithms against AERONET data in Arctic environments and they found that ACOLITE provided good estimates of Aerosol Optical Thickness and more accurate spectra between 490 and 783 nm. They also found that ACOLITE dealt better with the adjacency effects caused by the high contrasts found in an Arctic environment. Although ACOLITE demonstrated lower overall errors in AC (Table 3), POLYMER produced a stronger linear

TABLE 5 Coefficients per atmospheric correction and respective performance statistics.

| AC | a | $b_1$ | $b_2$ | $b_3$ | $R^2$ | MAPE % | RMSE ($sr^{-1}$) | SSPB % | MdSA % |
|---|---|---|---|---|---|---|---|---|---|
| ACOLITE | 0.0219 | −0.2589 | −0.0980 | 0.5211 | 0.88 | 17.04 | 0.0097 | −2.00 | 12.62 |
| POLYMER | 0.1223 | −0.1079 | −0.0909 | 0.2588 | 0.99 | 3.48 | 0.0028 | 0.94 | 3.20 |
| C2RCC | 0.0167 | 2.5785 | 0.0945 | −2.8038 | 0.96 | 3.09 | 0.0030 | 0 | 3.02 |

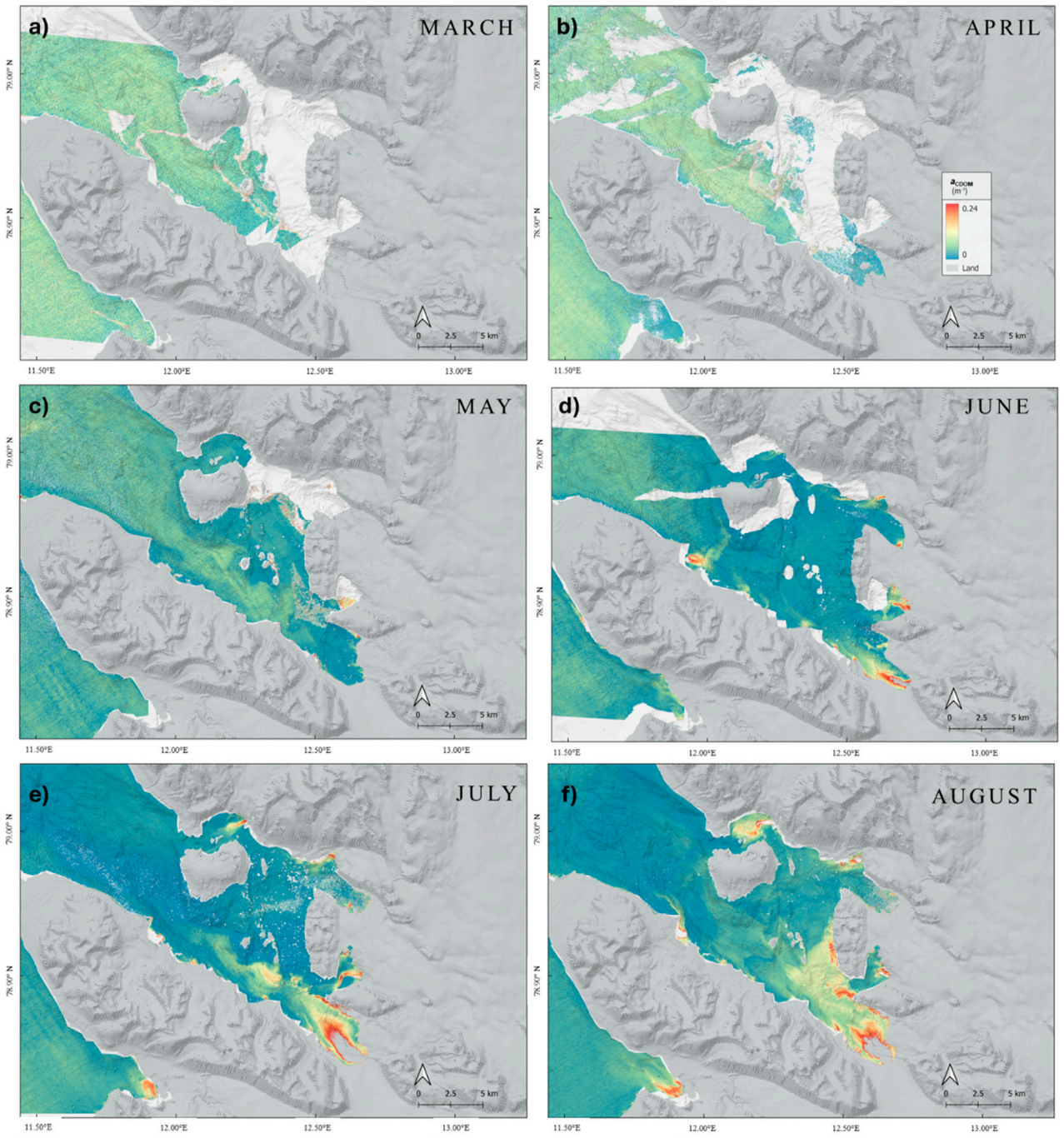


FIGURE 8
Sentinel-2 MSI imagery processed with Polymer AC and Kongsfjorden algorithm showing aCDOM (m-1) values for six different days in 2023: **(a)** 24th March, **(b)** 23rd April, **(c)** 27th May, **(d)** 21st June, **(e)** 08th July, and **(f)** 26th August.

calibration model for our tuned $a_{CDOM}$ $(443)_{KB}$ (Figures 10a,b) and lower errors. This suggests that POLYMER errors, while larger, are systematic and linear, allowing the regression model to compensate for them effectively. In contrast, ACOLITE errors in AC, though smaller on average, appear to be more inconsistent, especially when compared to the 490 nm band, which is used as a common denominator. This highlights the importance of evaluating the full retrieval chain rather than assuming the best-performing AC will lead to the best final product. However, CDOM retrievals using ACOLITE were comparable to the ones produced by POLYMER. In this study we selected POLYMER because it gave slightly better CDOM retrievals ($R^2$ = 0.99 vs. 0.88). Finally, even though C2RCC showed good results for the re-calibrated $a_{CDOM}$ $(443)_{KB,}$ it completely failed to resolve the highly sea-ice/glacier influenced station (KB5G), reducing the number of matchups to four (Figure 10c).

When benchmarked against our *in situ* hyperspectral data, a clear performance trend emerged among different algorithms.

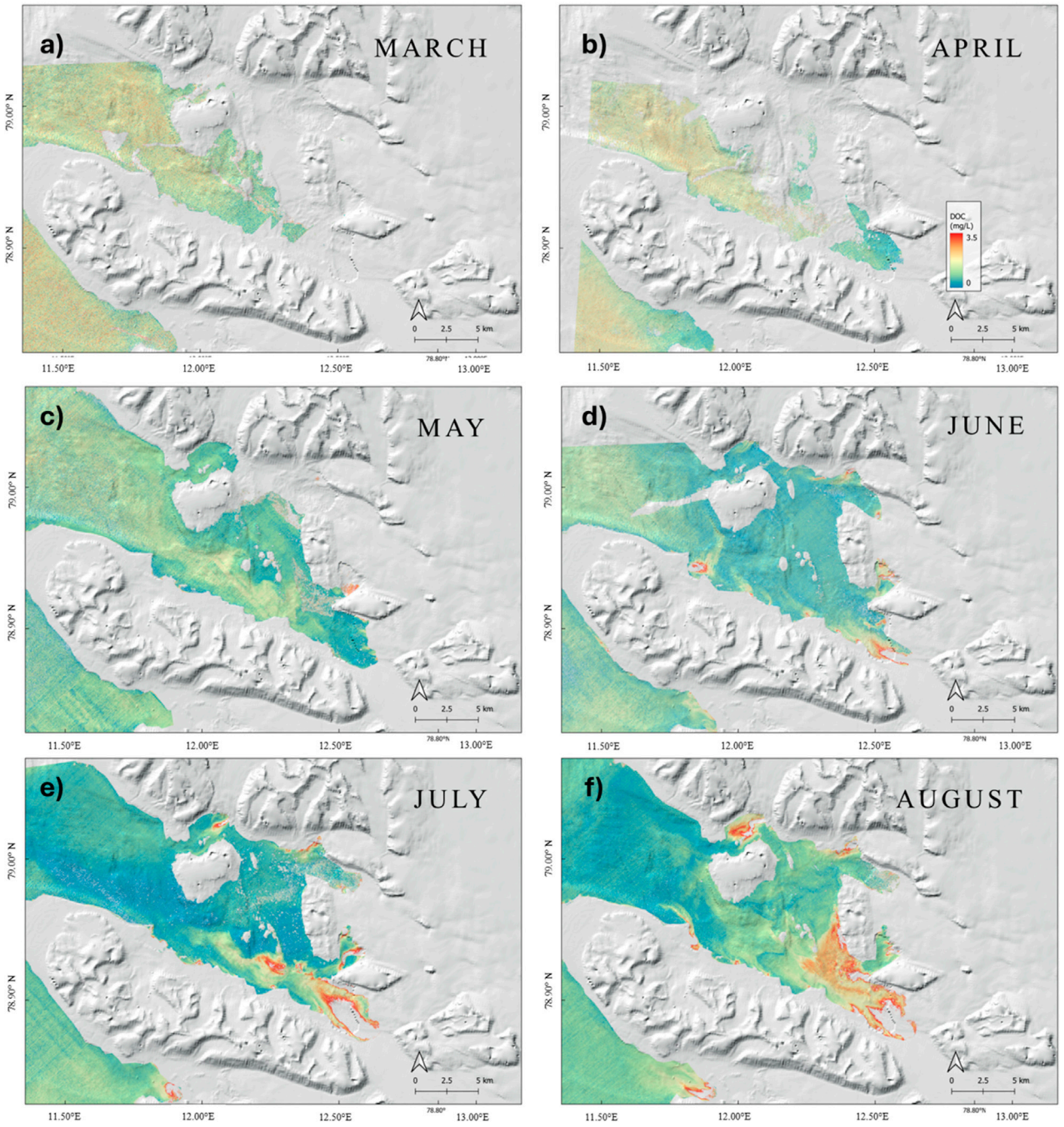


FIGURE 9
Sentinel-2 MSI images showing DOC (mg/L) derived from the tuned $a_{CDOM}$ (443) algorithm for six different days in 2023: **(a)** 24th March, **(b)** 23rd April, **(c)** 27th May, **(d)** 21st June, **(e)** 08th July, and **(f)** 26th August.

Models employing a band-ratio approach with shorter wavelengths, such as SHA11A and LIU21, performed best. This success is likely because the $a_{CDOM}$ absorption signal is exponentially strongest at these shorter wavelengths, providing a clearer target. By ratioing a high-signal blue band against a longer wavelength band, these models effectively minimize errors from residual atmospheric effects and particulate backscattering. In contrast, algorithms more dependent on longer wavelengths (e.g., FIC11, BR15) produced the poorest $a_{CDOM}$ (440) retrievals. In these optically complex glacial waters, the signal in the green and red spectrum is often dominated by scattering from suspended sediment, confounding the retrieval of the true $a_{CDOM}$ signature (Kavan et al., 2022). The site-specific nature of these relationships is a recurring theme. For instance, Mascarenhas and Zielinski (2019) showed that empirical coefficients developed for one fjord failed in an adjacent system, underscoring the critical need for localized calibration.

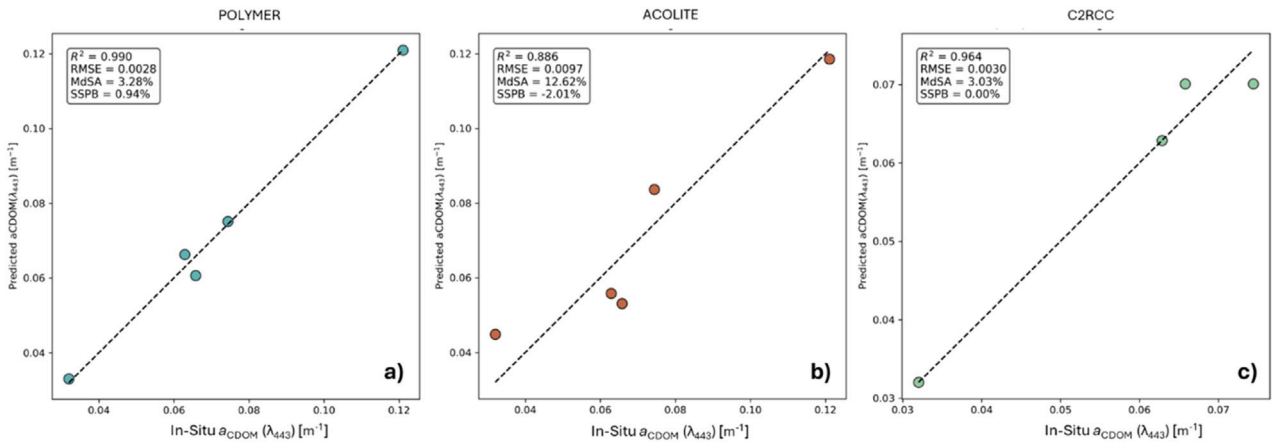


FIGURE 10
$a_{CDOM}443_{KB}$ model y-axis vs. resampled Sentinel-2 MSI reflectance x-axis for three AC: Polymer **(a)**, Acolite **(b)** and C2RCC **(c)**.

Regarding the relationship between $a_{CDOM}$ and DOC, reported linear correlations vary significantly (Matsuoka et al., 2013). *In situ* measurements show coefficients as high as 0.97, whereas satellite-derived estimates can drop to 0.53, with DOC errors reaching up to 50% in some cases. Regional differences, such as those observed between the Southern Beaufort Sea, Laptev Sea, and areas impacted by river plumes. For example, the influence of total suspended matter and sediment resuspension can lead to co-variation with $a_{CDOM}$, complicating DOC estimation (Juhls et al., 2019). Additionally, temporal mismatches (exceeding ±60 h), water type variability, low marine reflectance and adjacency effects, especially in near-shore and ice-affected waters (IOCCG, 2010; Tilstone et al., 2021; Juhls et al., 2022) and seasonal shifts (e.g., during ice melt and freshet), further complicate the ability to transfer a single DOC-CDOM relationship across the Arctic (Matsuoka et al., 2013). The scarcity of *in-situ* data, particularly for under-ice conditions, further hinders model development and validation. While high spatial resolution sensors like Sentinel-2 and Landsat 8 have shown good results, their performance in CDOM and DOC retrievals remain moderate. For example, Mabit et al. (2022) achieved ~45% accuracy for CDOM using red-to-green band ratios, while Ansper-Toomsalu et al. (2024) reported large biases across multiple AC schemes. Even algorithms specifically designed for these environments, like the Arctic Nearshore Turbidity Algorithm (Klein et al., 2021), face limitations from sensor resolution. Sentinel-3's coarse spatial resolution (300 m), for instance, are inadequate for resolving the narrow and dynamic plumes characteristic of fjords. Ultimately, the complex interplay of permafrost thaw, glacial runoff, and coastal erosion drives an optical variability that limits the direct transferability of standard algorithms (Straneo et al., 2019). The poor performance of published models (Table 4) demonstrates that a simple band-ratio algorithm is insufficient. Our analysis strongly suggests that the inclusion of the R704/R490 ratio is critical (Supplementary Appendix 1). While the 704 nm band has no direct physical link to $a_{CDOM}$, its inclusion likely acts as a crucial correction term for a co-varying property, such as high scattering from glacial sediments. In these optically complex waters, the 704 nm band is highly sensitive to particle scattering. By including this ratio, the model can de-couple the scattering signal from the absorption signal, allowing the other ratios (e.g., R664/R490 to more accurately capture the variability in CDOM (Supplementary Appendix 1). Despite these challenges, our work demonstrates that plausible $a_{CDOM}$ retrievals from Sentinel-2 MSI are achievable; the provided algorithm is regionally tuned and leverages the spectral bands where the CDOM signal is dominant. More *in-situ* $R_{rs}$ and CDOM data can be obtained in future research works to further validate and/or improve the robustness of CDOM retrieving algorithm.

## 4.2 Factors affecting CDOM-DOC relationships

The relationship between CDOM and DOC is crucial for biogeochemical $R_{rs}$ but is subject to significant challenges. Consistent with previous work (e.g., Connolly et al., 2021; Juhls et al., 2019), our data show a progressive increase in the CDOM-DOC concentration from March to August, coinciding with the transition to open-water conditions. In spring (March–April), CDOM levels were moderate and spatially uniform. By summer, background open-water CDOM had decreased, but distinct high-CDOM plumes from marine-terminating glaciers created a much patchier optical landscape, reflecting shifting sources and processing of organic matter (OM).

Previous studies have shown that during the spring freshet, terrestrial inputs from rivers dominate, leading to a tight coupling between CDOM and DOC (Para et al., 2013). However, this relationship often weakens under sea-ice or during shoulder seasons as DOM ages and undergoes photochemical and microbial processing. Furthermore, the sources themselves may change; for example, nitrogen-rich compounds released from sea-ice can produce $a_{CDOM}$ signatures that peak below 400 nm (Aguilar Vega et al., 2025, unpublished). In fjords where autochthonous production is a major source of DOC, CDOM and DOC can

decouple entirely (Connolly et al., 2021). These factors limit the universal applicability of CDOM-based DOC proxies. Additionally, the strong longitudinal gradients observed from river mouths to offshore waters (Juhls et al., 2019) highlight the necessity of local calibration for $R_{rs}$ algorithms. For example, Matsuoka et al. (2013) achieved high accuracy ($r^2$ up to 0.98) for oceanic samples using a semi-analytical approach, but performance dropped in turbid or coastal waters unless parameters were regionally adapted. Reliable DOC retrievals also depend on cloud- and ice-free imagery, a significant challenge in the Arctic. This immense seasonal variability creates wide shifts in the magnitude of $a_{CDOM}$ undermining the reliability of static, one-size-fits-all $R_{rs}$ models. To reduce retrieval errors, particularly during periods of rapid optical transition, algorithms must be seasonally parameterised or dynamically adjusted using near real-time field data (Mascarenhas and Zielinski, 2019). Moreover, the lack of ultraviolet bands (<400 nm) on sensors like Sentinel-2 MSI means they likely miss a fraction of the total CDOM signal. Future satellite missions with UV capabilities could therefore markedly improve DOC estimation in these regions.

# 5 Conclusion

CDOM absorbed more than half of the incoming blue light at every station, even at the Chla peak. NAP exceeded 80% of absorption, mainly in the inner fjord where tide water glaciers' influence was stronger. CDOM, mineral loads and vertical structure vary strongly over kilometres and days; empirical $R_{rs}$ relationships must be calibrated inside each fjord and periodically re-evaluated. A single "Arctic" or "high latitude" tuning is insufficient, seasonal parameterisation is essential. Spring melt, midsummer photobleaching and autumn resuspension quickly shift the CDOM-DOC coupling making a challenge the use of transferable models.

Accurately resolving CDOM is more than a retrieval precision: model studies show that the additional absorption it provides can raise under-ice heat content by >1 °C (Hill and Zimmerman, 2016), therefore, improving CDOM algorithms directly benefits Arctic heat-budget assessments, carbon-cycle estimates and ecosystem forecasts. We therefore recommend:

1. Fjord-specific optical calibration: Recalibrate algorithms inside each fjord so that CDOM spectra, mineral absorption, and depth-layered phytoplankton signals are set by local measurements, not regional averages.
2. Near UV/blue-capable satellites: Use of forthcoming sensors (NASA PACE, SBG; ESA LSTM) that push coverage below 400 nm, the range needed to isolate the highly variable CDOM fractions of early-spring freshet waters.
3. Year-round *in-situ* radiometry: Increase efforts and collaborations with local communities to keep autonomous radiometer moorings running and run targeted ship/ice campaigns through every season to validate retrievals under ice and plume regimes, and update coefficients as optics shift.

Implementing these three measures will reduce retrieval uncertainties to the threshold needed for reliable, year-round monitoring of Arctic coastal ecosystems increasingly shaped by sea-ice loss, glacial runoff, and sediment plumes.

# Data availability statement

The raw data supporting the conclusions of this article will be made available by the authors, without undue reservation.

# Author contributions

XA: Conceptualization, Formal Analysis, Funding acquisition, Investigation, Methodology, Project administration, Resources, Validation, Visualization, Writing – original draft, Writing – review and editing. DJ: Data curation, Supervision, Validation, Writing – review and editing. AF: Funding acquisition, Resources, Writing – review and editing. MC: Funding acquisition, Resources, Writing – review and editing. II: Resources, Writing – review and editing. AK: Funding acquisition, Resources, Writing – review and editing. CC: Supervision, Writing – review and editing. ES: Conceptualization, Data curation, Formal Analysis, Investigation, Methodology, Resources, Software, Supervision, Validation, Visualization, Writing – review and editing.

# Funding

The authors declare that financial support was received for the research and/or publication of this article. This research was possible through the generous support of the SAGES SALTIRE Emerging Researcher Scheme (2023), which funded the project "Implications of glacial organic carbon on the marine net primary production in the most rapidly warming place on Earth: the Svalbard archipelago," with the grant ID: PO 20315773. The study was also supported by the project CLEAN within the FRAM High North Research Centre for Climate and the Environment (The Fram Centre), and ESA Climate Change Initiative (CCI) Lakes.

# Conflict of interest

The authors declare that the research was conducted in the absence of any commercial or financial relationships that could be construed as a potential conflict of interest.

The author(s) declared that they were an editorial board member of Frontiers, at the time of submission. This had no impact on the peer review process and the final decision.

# Generative AI statement

The author(s) declare that no Generative AI was used in the creation of this manuscript.

Any alternative text (alt text) provided alongside figures in this article has been generated by Frontiers with the support of artificial intelligence and reasonable efforts have been made to ensure

accuracy, including review by the authors wherever possible. If you identify any issues, please contact us.

## Publisher's note

All claims expressed in this article are solely those of the authors and do not necessarily represent those of their affiliated organizations, or those of the publisher, the editors and the reviewers. Any product that may be evaluated in this article, or claim that may be made by its manufacturer, is not guaranteed or endorsed by the publisher.

## Supplementary material

The Supplementary Material for this article can be found online at: https://www.frontiersin.org/articles/10.3389/frsen.2025.1703604/full#supplementary-material

## References


Aguilar Vega, X., Fransson, A., Melissa, C., Washbourne, I., and Spyrakos, E. (2025). Carbon in an arctic fjord: sea-ice carbon transformations, and $CO_2$ linkages. *Front. Mar. Sci.* 12, 1688237. doi:10.3389/fmars.2025.1688237

Amon, R. M. W., Kaiser, K., and Engel, A. (2024). Dissolved organic matter in the Arctic Ocean. *Biogeochem. Mar. Dissolved Org. Matter*, 693–737. doi:10.1016/B978-0-443-13858-4.00017-4

Ansper-Toomsalu, A., Uusõue, M., Kangro, K., Hieronymi, M., and Alikas, K. (2024). Suitability of different in-water algorithms for eutrophic and absorbing waters applied to Sentinel-2 MSI and Sentinel-3 OLCI data. *Front. Remote Sens.* 5, 1423332. doi:10.3389/frsen.2024.1423332

Aurin, D., Mannino, A., and Lary, D. J. (2018). Remote sensing of CDOM, CDOM spectral slope, and dissolved organic carbon in the global ocean. *Appl. Sci. Switz.* 8 (12), 2687. doi:10.3390/app8122687

Brezonik, P. L., Olmanson, L. G., Finlay, J. C., and Bauer, M. E. (2015). Factors affecting the measurement of CDOM by remote sensing of optically complex inland waters. *Remote Sens. Environ.* 157, 199–215. doi:10.1016/J.RSE.2014.04.033

Bruhwiler, L., Parmentier, F.-J. W., Crill, P., Leonard, M., and Palmer, P. I. (2021). The arctic carbon cycle and its response to changing climate. *Curr. Clim. Change Rep.* 7 (1), 14–34. doi:10.1007/s40641-020-00169-5

Burggraaff, O. (2020). Biases from incorrect reflectance convolution. *Opt. Express* 28 (9), 13801–13816. doi:10.1364/OE.391470

Cao, N., Lin, X., Liu, C., Tan, M. L., Shi, J., Jim, C. Y., et al. (2024). Estimation of dissolved organic carbon using Sentinel-2 in the eutrophic Lake ebinur, China. *Remote Sens.* 16 (2), 252. doi:10.3390/rs16020252

Castellani, G., Veyssière, G., Karcher, M., Stroeve, J., Banas, S. N., Bouman, A. H., et al. (2022). Shine a light: under-ice light and its ecological implications in a changing Arctic Ocean. *Ambio* 51 (2), 307–317. doi:10.1007/s13280-021-01662-3

Chifflard, P., Fasching, C., Reiss, M., Ditzel, L., and Boodoo, K. S. (2019). Dissolved and particulate organic carbon in icelandic proglacial streams: a first estimate. *WaterSwitzerl.* 11 (4), 748. doi:10.3390/w11040748

Clark, J. B., Mannino, A., Tzortziou, M., Spencer, R. G. M., and Hernes, P. (2022). The transformation and export of organic carbon across an arctic river-delta-ocean continuum. *J. Geophys. Res. Biogeosciences* 127 (12), e2022JG007139. doi:10.1029/2022JG007139

Coble, P. G. (2007). Marine optical biogeochemistry: the chemistry of ocean color. *Chem. Rev.* 107, 402–418. doi:10.1021/cr050350

Comiso, J. C. (1991). Satellite remote sensing of the polar oceans. *J. Mar. Syst.* 2 (3-4), 395–434. doi:10.1016/0924-7963(91)90044-u

Comiso, J. C. (2015). Variability and trends of global sea ice cover and sea level: effects on physicochemical parameters. *Clim. Change Mar. Freshw. Toxins*, 1–34.

Connolly, C. T., Crump, B. C., Dunton, K. H., and McClelland, J. W. (2021). Seasonality of dissolved organic matter in lagoon ecosystems along the Alaska beaufort sea coast. *Limnol. Oceanogr.* 66 (12), 4299–4313. doi:10.1002/lno.11962

Cottier, F., Tverberg, V., Inall, M., Svendsen, H., Nilsen, F., and Griffiths, C. (2005). Water mass modification in an arctic fjord through cross-shelf exchange: the seasonal hydrography of kongsfjorden, Svalbard. *J. Geophys. Res. Oceans* 110 (12), 1–18. doi:10.1029/2004JC002757

Efimova, T., Churilova, T., Skorokhod, E., Suslin, V., Buchelnikov, A. S., Glukhovets, D., et al. (2023). Light absorption by optically active components in the arctic region (august 2020) and the possibility of application to satellite products for water quality assessment. *Remote Sens.* 15 (17), 4346. doi:10.3390/rs15174346

El Kassar, J., Juhls, B., Hieronymi, M., Preusker, R., Morgenstern, A., Fischer, J., et al. (2023). Optical remote sensing (Sentinel-3 OLCI) used to monitor dissolved organic carbon in the lena river, Russia. *Front. Mar. Sci.* 10, 1082109. doi:10.3389/fmars.2023.1082109

Feng, D., Gleason, C. J., Lin, P., Yang, X., Pan, M., and Ishitsuka, Y. (2021). Recent changes to arctic river discharge. *Nat. Commun.* 12 (1), 6917. doi:10.1038/s41467-021-27228-1

Ficek, D., Zapadka, T., and Dera, J. (2011). Remote sensing reflectance of Pomeranian Lakes and the Baltic. *Oceanologia* 53 (4), 959–970. doi:10.5697/OC.53-4.959

Fichot, C. G., and Benner, R. (2011). A novel method to estimate DOC concentrations from CDOM absorption coefficients in coastal waters. *Geophys. Research Letters* 38 (3). doi:10.1029/2010gl046152

Fichot, C. G., Tzortziou, M., and Mannino, A. (2023). Remote sensing of dissolved organic carbon (DOC) stocks, fluxes and transformations along the land-ocean aquatic continuum: advances, challenges, and opportunities. *Earth-Science Rev.* 242, 104446. doi:10.1016/j.earscirev.2023.104446

Gabarró, C., Hughes, N., Wilkinson, J., Bertino, L., Bracher, A., Diehl, T., et al. (2023). Improving satellite-based monitoring of the polar regions: identification of research and capacity gaps. *Front. Remote Sens.* 4, 952091. doi:10.3389/frsen.2023.952091

Glukhovets, D. I., Salyuk, P. A., Artemiev, V. A., Shtraikhert, E. A., and Zakharkov, S. P. (2021). Variability of bio-optical characteristics of surface water layer during transatlantic transect in 2019–2020. *Oceanology* 61 (6), 872–880. doi:10.1134/S0001437021060229

Glukhovets, D., Sheberstov, S., Vazyulya, S., Yushmanova, A., Salyuk, P., Sahling, I., et al. (2022). Influence of the accuracy of chlorophyll-retrieval algorithms on the estimation of solar radiation absorbed in the Barents Sea. *Remote Sens.* 14 (19), 4995. doi:10.3390/rs14194995

Gonçalves-Araujo, R., Granskog, M. A., Bracher, A., Azetsu-Scott, K., Dodd, P. A., and Stedmon, C. A. (2016). Using fluorescent dissolved organic matter to trace and distinguish the origin of arctic surface waters. *Sci. Rep.* 6 (1), 33978. doi:10.1038/srep33978

Goncalves-Araujo, R., Rabe, B., Peeken, I., and Bracher, A. (2018). High colored dissolved organic matter (CDOM) absorption in surface waters of the central-eastern Arctic Ocean: implications for biogeochemistry and ocean color algorithms. *PloS One* 13 (1), e0190838. doi:10.1371/journal.pone.0190838

Herrault, P. A., Gandois, L., Gascoin, S., Tananaev, N., Le Dantec, T., and Teisserenc, R. (2016). Using high spatio-temporal optical remote sensing to monitor dissolved organic carbon in the arctic river yenisei. *Remote Sens.* 8 (10), 803. doi:10.3390/rs8100803

Hieronymi, M., Bi, S., Müller, D., Schütt, E. M., Behr, D., Brockmann, C., et al. (2023). Ocean color atmospheric correction methods in view of usability for different optical water types. *Front. Mar. Sci.* 10, 1129876. doi:10.3389/fmars.2023.1129876

Hill, V. J., and Zimmerman, R. C. (2016). Characteristics of colored dissolved organic material in first year landfast sea ice and the underlying water column in the Canadian arctic in the early spring. *Mar. Chem.* 180, 1–13. doi:10.1016/j.marchem.2016.01.007

Holmes, F. A., van Dongen, E., Noormets, R., Pętlicki, M., and Kirchner, N. (2023). Impact of tides on calving patterns at kronebreen, Svalbard–insights from three-dimensional ice dynamical modelling. *Cryosphere* 17 (5), 1853–1872. doi:10.5194/tc-17-1853-2023

Hop, H., and Wiencke, C. (2019). "The ecosystem of kongsfjorden, Svalbard," in *The ecosystem of kongsfjorden, Svalbard* (Cham: Springer International Publishing), 1–20.

Huang, J., Wu, M., Cui, T., and Yang, F. (2019). Quantifying DOC and its controlling factors in major arctic rivers during ice-free conditions using Sentinel-2 data. *Remote Sens.* 11 (24), 2904. doi:10.3390/rs11242904

IOCCG (2010). "Atmospheric correction for remotely-sensed ocean-colour products," in *Canada, international ocean-colour coordinating group (IOCCG)*. Editors Wang, M., and Dartmouth, N. S., 78pp. doi:10.25607/OBP-101

Irrgang, A. M., Bendixen, M., Farquharson, L. M., Baranskaya, A. V., Erikson, L. H., Gibbs, A. E., et al. (2022). Drivers, dynamics and impacts of changing arctic coasts. *Nat. Rev. Earth Environ.* 3 (1), 39–54. doi:10.1038/s43017-021-00232-1

Jamal, M., Tiantian, G., Li, F., and Liu, Y. (2025). Glacial retreat and climate change: insights from remote sensing technologies. *Environ. Sci. Pollut. Res.* 32 (25), 15034–15049. doi:10.1007/s11356-025-36578-y

Juhls, B., Overduin, P. P., Hölemann, J., Hieronymi, M., Matsuoka, A., Heim, B., et al. (2019). Dissolved organic matter at the fluvial–marine transition in the laptev sea using

*in situ* data and ocean colour remote sensing. *Biogeosciences* 16 (13), 2693–2713. doi:10.5194/bg-16-2693-2019

Juhls, B., Matsuoka, A., Lizotte, M., Bécu, G., Overduin, P. P., El Kassar, J., et al. (2022). Seasonal dynamics of dissolved organic matter in the mackenzie Delta, Canadian arctic waters: implications for ocean colour remote sensing. *Remote Sens. Environ.* 283, 113327. doi:10.1016/j.rse.2022.113327

Kavan, J., Wieczorek, I., Tallentire, G. D., Demidionov, M., Uher, J., and Strzelecki, M. C. (2022). Estimating suspended sediment fluxes from the largest glacial lake in Svalbard to fjord system using Sentinel-2 data: trebrevatnet case study. *Water* 14 (12), 1840. doi:10.3390/w14121840

Kirk, J. T. O. (1975). A theoretical analysis of the contribution of algal cells to the attenuation of light within natural waters i. general treatment of suspensions of pigmented cells. *New Phytol.* 75 (1), 11–20. doi:10.1111/j.1469-8137.1975.tb01366.x

Kishino, M., Takahashi, M., Okami, N., and Ichimura, S. (1985). Estimation of the spectral absorption coefficients of phytoplankton in the sea. *Bull. Mar. Sci.* 37 (2), 634–642.

Klein, K. P., Lantuit, H., Heim, B., Doxaran, D., Juhls, B., Nitze, I., et al. (2021). The arctic nearshore turbidity algorithm (ANTA)-A multi sensor turbidity algorithm for arctic nearshore environments. *Sci. Remote Sens.* 4, 100036. doi:10.1016/j.srs.2021.100036

Kohler, J., James, T. D., Murray, T., Nuth, C., Brandt, O., Barrand, N. E., et al. (2007). Acceleration in thinning rate on Western Svalbard glaciers. *Geophys. Res. Lett.* 34 (18). doi:10.1029/2007GL030681

König, M., Hieronymi, M., and Oppelt, N. (2019). Application of sentinel-2 MSI in arctic research: evaluating the performance of atmospheric correction approaches over arctic sea ice. *Front. Earth Sci.* 7, 22. doi:10.3389/feart.2019.00022

Lee, Z., Carder, K. L., and Arnone, R. A. (2002). Deriving inherent optical properties from water color: a multiband quasi-analytical algorithm for optically deep waters. *Appl. Optics* 41 (27), 5755–5772. doi:10.1364/ao.41.005755

Lewis, K. M., Mitchell, B. G., Van Dijken, G. L., and Arrigo, K. R. (2016). Regional chlorophyll a algorithms in the Arctic Ocean and their effect on satellite-derived primary production estimates. *Deep Sea Res. Part II Top. Stud. Oceanogr.* 130, 14–27. doi:10.1016/j.dsr2.2016.04.020

Liu, G., Li, S., Song, K., Wang, X., Wen, Z., Kutser, T., et al. (2021). Remote sensing of CDOM and DOC in alpine Lakes across the Qinghai-Tibet Plateau using Sentinel-2A imagery data. *J. Environ. Manag.* 286, 112231. doi:10.1016/j.jenvman.2021.112231

Lucas, S., Johannessen, J. A., Cancet, M., Pettersson, L. H., Esau, I., Rheinlænder, J. W., et al. (2023). Knowledge gaps and impact of future satellite missions to facilitate monitoring of changes in the Arctic Ocean. *Remote Sens.* 15 (11), 2852. doi:10.3390/rs15112852

Mabit, R., Araújo, C. A. S., Singh, R. K., and Bélanger, S. (2022). Empirical remote sensing algorithms to retrieve SPM and CDOM in Québec coastal waters. *Front. Remote Sens.* 3, 834908. doi:10.3389/frsen.2022.834908

Mannino, A., Russ, M. E., and Hooker, S. B. (2008). Algorithm development and validation for satellite-derived distributions of DOC and CDOM in the US middle Atlantic bight. *J. Geophys. Res. Oceans* 113 (C7). doi:10.1029/2007jc004493

Mascarenhas, V. J., and Zielinski, O. (2019). Hydrography-driven optical domains in the vaigat-disko Bay and godthabsfjord: effects of glacial meltwater discharge. *Front. Mar. Sci.* 6, 335. doi:10.3389/fmars.2019.00335

Matsuoka, A., Hooker, S. B., Bricaud, A., Gentili, B., and Babin, M. (2013). Estimating absorption coefficients of colored dissolved organic matter (CDOM) using a semi-analytical algorithm for southern beaufort sea waters: application to deriving concentrations of dissolved organic carbon from space. *Biogeosciences* 10 (2), 917–927. doi:10.5194/bg-10-917-2013

Matsuoka, A., Ortega-Retuerta, E., Bricaud, A., Arrigo, K. R., and Babin, M. (2015). Characteristics of colored dissolved organic matter (CDOM) in the Western Arctic Ocean: relationships with microbial activities. *Deep Sea Res. Part II Top. Stud. Oceanogr.* 118, 44–52. doi:10.1016/j.dsr2.2015.02.012

Nguyen, V. S., Loisel, H., Vantrepotte, V., Mériaux, X., and Tran, D. L. (2024). An empirical algorithm for estimating the absorption of colored dissolved organic matter from Sentinel-2 (MSI) and Landsat-8 (OLI) observations of coastal waters. *Remote Sens.* 16 (21), 4061. doi:10.3390/rs16214061

Opsahl, S., Benner, R., and Amon, R. M. W. (1999). Major flux of terrigenous dissolved organic matter through the Arctic Ocean. *Limnol. Oceanogr.* 44 (8), 2017–2023. doi:10.4319/lo.1999.44.8.2017

Pahlevan, N., Chittimalli, S. K., Balasubramanian, S. V., and Vellucci, V. (2019). Sentinel-2/Landsat-8 product consistency and implications for monitoring aquatic systems. *Remote Sens. Environ.* 220, 19–29. doi:10.1016/j.rse.2018.10.027

Pahlevan, N., Mangin, A., Balasubramanian, S. V., Smith, B., Alikas, K., Arai, K., et al. (2021). ACIX-Aqua: a global assessment of atmospheric correction methods for Landsat-8 and Sentinel-2 over lakes, rivers, and coastal waters. *Remote Sens. Environ.* 258, 112366. doi:10.1016/j.rse.2021.112366

Para, J., Charrière, B., Matsuoka, A., Miller, W. L., Rontani, J.-F., and Sempere, R. (2013). UV/PAR radiation and DOM properties in surface coastal waters of the Canadian shelf of the beaufort sea during summer 2009. *Biogeosciences* 10 (4), 2761–2774. doi:10.5194/bg-10-2761-2013

Peterson, B. J., Holmes, R. M., Mcclelland, J. W., Vörösmarty, C. J., Lammers, R. B., Shiklomanov, A. I., et al. (2002). Increasing river discharge to the Arctic Ocean. *Sci. (1979).* 298, 2171–2173. doi:10.1126/science.1077445

Renosh, P. R., Doxaran, D., De Keukelaere, L., and Gossn, J. I. (2020). Evaluation of atmospheric correction algorithms for sentinel-2-MSI and sentinel-3-OLCI in highly turbid estuarine waters. *Remote Sens.* 12 (8), 1285. doi:10.3390/RS12081285

Sandven, H., Granskog, M. A., Opdal, A. F., Connan-McGinty, S., Hamre, B., and McKee, D. (2025). Increased light availability in the northern Barents Sea driven by sea ice loss. *J. Geophys. Res. Oceans* 130 (6), e2025JC022370. doi:10.1029/2025JC022370

Schuler, T. V., Kohler, J., Elagina, N., Hagen, J. O. M., Hodson, A. J., Jania, J. A., et al. (2020). Reconciling Svalbard glacier mass balance. *Front. Earth Sci.* 8, 156. doi:10.3389/feart.2020.00156

Seegers, B. N., Stumpf, R. P., Schaeffer, B. A., Loftin, K. A., and Werdell, P. J. (2018). Performance metrics for the assessment of satellite data products: an ocean color case study. *Opt. Express* 26 (6), 7404–7422. doi:10.1364/OE.26.007404

Sevestre, H., Benn, D. I., Hulton, N. R. J., and Bælum, K. (2015). Thermal structure of Svalbard glaciers and implications for thermal switch models of glacier surging. *J. Geophys. Res. Earth Surf.* 120 (10), 2220–2236. doi:10.1002/2015jf003517

Shanmugam, P. (2011). New models for retrieving and partitioning the colored dissolved organic matter in the global ocean: implications for remote sensing. *Remote Sens. Environ.* 115 (6), 1501–1521. doi:10.1016/J.RSE.2011.02.009

Shen, Y., Benner, R., Robbins, L. L., and Wynn, J. G. (2016). Sources, distributions, and dynamics of dissolved organic matter in the Canada and makarov basins. *Front. Mar. Sci.* 3, 198. doi:10.3389/fmars.2016.00198

Smith, G. C., Allard, R., Babin, M., Bertino, L., Chevallier, M., Corlett, G. K., et al. (2019). Polar ocean observations: a critical gap in the observing system and its effect on environmental predictions from hours to a season. *Front. Media S.A* 6 (Issue JUL), 429. doi:10.3389/fmars.2019.00429

Stedmon, C. A., Amon, R. M. W., Rinehart, A. J., and Walker, S. A. (2011). The supply and characteristics of colored dissolved organic matter (CDOM) in the Arctic Ocean: Pan arctic trends and differences. *Mar. Chem.* 124 (1–4), 108–118. doi:10.1016/j.marchem.2010.12.007

Steinmetz, F., and Ramon, D. (2018). Sentinel-2 MSI and Sentinel-3 OLCI consistent ocean colour products using POLYMER. *Remote Sens. Open Coast. Ocean Inland Waters* 10778, 46–55.

Stramski, D., Reynolds, R. A., Kaczmarek, S., Uitz, J., and Zheng, G. (2015). Correction of pathlength amplification in the filter-pad technique for measurements of particulate absorption coefficient in the visible spectral region. *Appl. Opt.* 54 (22), 6763–6782. doi:10.1364/AO.54.006763

Straneo, F., Sutherland, D. A., Stearns, L., Catania, G., Heimbach, P., Moon, T., et al. (2019). The case for a sustained Greenland ice sheet-ocean observing system (GrIOOS). *Front. Mar. Sci.* 6 (Issue MAR), 138. doi:10.3389/fmars.2019.00138

Sun, X., Zhang, Y., Zhang, Y., Shi, K., Zhou, Y., and Li, N. (2021). Machine learning algorithms for chromophoric dissolved organic matter (CDOM) estimation based on landsat 8 images. *Remote Sens.* 13 (18), 3560. doi:10.3390/rs13183560

Svendsen, H., Beszczynska-Møller, A., Hagen, J. O., Lefauconnier, B., Tverberg, V., Gerland, S., et al. (2002). The physical environment of kongsfjorden–krossfjorden, an arctic fjord system in Svalbard. *Polar Res.* 21 (1), 133–166. doi:10.1111/j.1751-8369.2002.tb00072.x

Tessin, E., Hamre, B., and Kristoffersen, A. S. (2024). Testing the limits of atmospheric correction over turbid Norwegian fjords. *Remote Sens.* 16 (21), 4082. doi:10.3390/rs16214082

Tilstone, G. H., Pardo, S., Simis, S. G., Qin, P., Selmes, N., Dessailly, D., et al. (2021). Consistency between satellite ocean colour products under high coloured dissolved organic matter absorption in the Baltic sea. *Remote Sens.* 14 (1), 89. doi:10.3390/rs14010089

Tiwari, S. P., and Shanmugam, P. (2011). An optical model for the remote sensing of coloured dissolved organic matter in coastal/ocean waters. *Estuar. Coast. Shelf Sci.* 93 (4), 396–402. doi:10.1016/J.ECSS.2011.05.010

Turner, J., and Overland, J. (2009). Contrasting climate change in the two polar regions. *Polar Res.* 28 (2), 146–164. doi:10.1111/j.1751-8369.2009.00128.x

Tverberg, V., Skogseth, R., Cottier, F., Sundfjord, A., Walczowski, W., Inall, M. E., et al. (2019). "The kongsfjorden transect: seasonal and inter-annual variability in hydrography," in *The ecosystem of kongsfjorden, Svalbard* (Springer), 49–104.

Tyler, A. N., Hunter, P. D., Spyrakos, E., Groom, S., Constantinescu, A. M., and Kitchen, J. (2016). Developments in Earth observation for the assessment and monitoring of inland, transitional, coastal and shelf-sea waters. *Sci. Total Environ.* 572, 1307–1321. doi:10.1016/j.scitotenv.2016.01.020

Vanhellemont, Q., and Ruddick, K. (2018). Atmospheric correction of metre-scale optical satellite data for inland and coastal water applications. *Remote Sensing Environment* 216, 586–597. doi:10.1016/j.rse.2018.07.015

Vantrepotte, V., Danhiez, F.-P., Loisel, H., Ouillon, S., Mériaux, X., Cauvin, A., et al. (2015). CDOM-DOC relationship in contrasted coastal waters: implication for DOC retrieval from ocean color remote sensing observation. *Opt. Express* 23 (1), 33–54. doi:10.1364/oe.23.000033

Vitousek, S., Buscombe, D., Vos, K., Barnard, P. L., Ritchie, A. C., and Warrick, J. A. (2023). The future of coastal monitoring through satellite remote sensing. *Camb. Prisms Coast. Futur.* 1, e10. doi:10.1017/cft.2022.4

Wadham, J. L., Hawkings, J. R., Tarasov, L., Gregoire, L. J., Spencer, R. G. M., Gutjahr, M., et al. (2019). Ice sheets matter for the global carbon cycle. *Nat. Commun.* 10 (1), 3567. doi:10.1038/s41467-019-11394-4

Warren, M. A., Simis, S. G. H., Martinez-Vicente, V., Poser, K., Bresciani, M., Alikas, K., et al. (2019). Assessment of atmospheric correction algorithms for the Sentinel-2A MultiSpectral imager over coastal and inland waters. *Remote Sens. Environ.* 225, 267–289. doi:10.1016/j.rse.2019.03.018

Zhang, S., Wang, D., Gong, F., Xu, Y., He, X., Zhang, X., et al. (2023). Evaluating atmospheric correction methods for sentinel– 2 in low– to– high–turbidity Chinese coastal waters. *Remote Sens.* 15 (9), 2353. doi:10.3390/rs15092353

Zheng, G., and DiGiacomo, P. M. (2017). Remote sensing of chlorophyll-a in coastal waters based on the light absorption coefficient of phytoplankton. *Remote Sens. Environ.* 201, 331–341. doi:10.1016/j.rse.2017.09.008

Zibordi, G., Johnson, B. C., Kwiatkowska, E., Voss, K. J., Antoine, D., Barnard, A., et al. (2025). System vicarious calibration for climate and global long-term operational ocean color applications. *Bull. Am. Meteorological Soc.* 106 (2), E394–E407. doi:10.1175/BAMS-D-24-0085.1

Zoffoli, M. L., Brando, V., Volpe, G., Vilas, L. G., Davies, B. F. R., Frouin, R., et al. (2025). CIAO: a machine-learning algorithm for mapping Arctic Ocean Chlorophyll-a from space. *Sci. Remote Sens.* 11, 100212. doi:10.1016/j.srs.2025.100212